A Possible Alignment Between the Orbits of Planetary Systems and their Visual Binary Companions

Sam Christian[1,2], Andrew Vanderburg[1,3], Juliette Becker[4,90], Daniel A. Yahalomi[5], Logan Pearce[6,91], George Zhou[7,8], Karen A. Collins[7], Adam L. Kraus[9], Keivan G. Stassun[10,11], Zoe de Beurs[1,9], George R. Ricker[1], Roland K. Vanderspek[1], David W. Latham[7], Joshua N. Winn[12], S. Seager[1,13,14], Jon M. Jenkins[15], Lyu Abe[16], Karim Agabi[16], Pedro J. Amado[17], David Baker[18], Khalid Barkaoui[19,20], Zouhair Benkhaldoun[20], Paul Benni[21], John Berberian[22], Perry Berlind[7], Allyson Bieryla[7], Emma Esparza-Borges[23,24], Michael Bowen[25,26], Peyton Brown[27], Lars A. Buchhave[28], Christopher J. Burke[1], Marco Buttu[29], Charles Cadieux[30], Douglas A. Caldwell[31], David Charbonneau[7], Nikita Chazov[32], Sudhish Chimaladinne[25], Kevin I. Collins[25], Deven Combs[25,33], Dennis M. Conti[34], Nicolas Crouzet[35], Jerome P. de Leon[36], Shila Deljookorani[37], Brendan Diamond[37], René Doyon[30,38], Diana Dragomir[39], Georgina Dransfield[40], Zahra Essack[13,41], Phil Evans[42], Akihiko Fukui[24,43], Tianjun Gan[44], Gilbert A. Esquerdo[7], Michaël Gillon[45], Eric Girardin[46], Pere Guerra[47], Tristan Guillot[16], Eleanor Kate K. Habich[48], Andreea Henriksen[28], Nora Hoch[48], Keisuke I Isogai[49,50], Emmanuël Jehin[51], Eric L. N. Jensen[52], Marshall C. Johnson[53], John H. Livingston[36], John F. Kielkopf[54], Kingsley Kim[25,33], Kiyoe Kawauchi[50], Vadim Krushinsky[32], Veronica Kunzle[37], Didier Laloum[55], Dominic Leger[37], Pablo Lewin[56], Franco Mallia[57], Bob Massey[58], Mayuko Mori[36], Kim K. McLeod[48], Djamel Mékarnia[16], Ismael Mireles[59], Nikolay Mishevskiy[60], Motohide Tamura[61,62,63], Felipe Murgas[64,65], Norio Narita[43,62,66,67,68], Ramon Naves[69], Peter Nelson[70], Hugh P. Osborn[1,71], Enric Palle[70,73], Hannu Parviainen[72,73], Peter Plavchan[25], Francisco J. Pozuelos[45,74], Markus Rabus[75], Howard M. Relles[7], Cristina Rodríguez López[17], Samuel N. Quinn[7], Francois-Xavier Schmider[16], Joshua E. Schlieder[76], Richard P. Schwarz[77], Avi Shporer[1], Laurie Sibbald[78,92], Gregor Srdoc[79], Caitlin Stibbards[25], Hannah Stickler[48], Olga Suarez[16], Chris Stockdale[80], Thiam-Guan Tan[81,82], Yuka Terada[83,84], Amaury Triaud[40], Rene Tronsgaard[28], William C. Waalkes[85], Gavin Wang[86,87], Noriharu Watanabe[50], Marie-Sainte Wenceslas[29], Geof Wingham[88], Justin Wittrock[25], and Carl Ziegler[89]

[1] Department of Physics and Kavli Institute for Astrophysics and Space Research, Massachusetts Institute of Technology, Cambridge, MA 02139, USA; samchristian@mit.edu
[2] Liberal Arts and Science Academy, Austin, TX 78724, USA
[3] Department of Astronomy, University of Wisconsin-Madison, Madison, WI 53706, USA
[4] Division of Geological and Planetary Sciences, California Institute of Technology, Pasadena, CA 91125, USA
[5] Department of Astronomy, Columbia University, 550 W 120th Street, New York, NY 10027, USA
[6] Steward Observatory, University of Arizona, Tucson, AZ 85721, USA
[7] Center for Astrophysics | Harvard & Smithsonian, 60 Garden Street, Cambridge, MA 02138, USA
[8] Centre for Astrophysics, University of Southern Queensland, Toowoomba, Queensland 4350, Australia
[9] Department of Astronomy, University of Texas at Austin, Austin, TX 78712, USA
[10] Department of Physics and Astronomy, Vanderbilt University, 6301 Stevenson Center Lane, Nashville, TN 37235, USA
[11] Department of Physics, Fisk University, 1000 17th Avenue North, Nashville, TN 37208, USA
[12] Department of Astrophysical Sciences, Princeton University, 4 Ivy Lane, Princeton, NJ 08544, USA
[13] Department of Earth, Atmospheric and Planetary Sciences, Massachusetts Institute of Technology, Cambridge, MA 02139, USA
[14] Department of Aeronautics and Astronautics, MIT, 77 Massachusetts Avenue, Cambridge, MA 02139, USA
[15] NASA Ames Research Center, Moffett Field, CA 94035, USA
[16] Université Côte d'Azur, Observatoire de la Côte d'Azur, CNRS, Laboratoire Lagrange, Bd de l'Observatoire, CS 34229, F-06304 Nice cedex 4, France
[17] Instituto de Astrofísica de Andalucía (IAA-CSIC), Glorieta de la Astronomía s/n, E-18008 Granada, Spain
[18] Physics Department, Austin College, Sherman, TX 75090, USA
[19] Astrobiology Research Unit, Université de Liège, 19C Allée du 6 Août, B-4000 Liège, Belgium
[20] Oukaimeden Observatory, High Energy Physics and Astrophysics Laboratory, Cadi Ayyad University, Marrakech, Morocco
[21] Acton Sky Portal (Private Observatory), Acton, MA, USA
[22] Woodson High School, 9525 Main St, Fairfax, VA 22031, USA
[23] Departamento de Astrofísica, Universidad de La Laguna (ULL), E-38206 La Laguna, Tenerife, Spain
[24] Instituto de Astrofísica de Canarias, Vía Láctea s/n, E-38205 La Laguna, Tenerife, Spain
[25] George Mason University, 4400 University Drive, Fairfax, VA 22030 USA
[26] Millennium Institute for Astrophysics, Chile
[27] Vanderbilt University, 2201 West End Avenue, Nashville, TN 37235, USA
[28] DTU Space, National Space Institute, Technical University of Denmark, Elektrovej 328, DK-2800 Kgs. Lyngby, Denmark
[29] PNRA, IPEV, Concordia Station, Antarctica
[30] Université de Montréal, Département de Physique, IREX, Montréal, QC H3C 3J7, Canada
[31] SETI Institute, Mountain View, CA 94043, USA
[32] Kourovka Observatory, Ural Federal University, 19 Mira street, Yekaterinburg, Russia
[33] Thomas Jefferson High School, for Science and Technology, 6560 Braddock Rd, Alexandria, VA 22312, USA
[34] American Association of Variable Star Observers, 49 Bay State Road, Cambridge, MA 02138, USA
[35] European Space Agency (ESA), European Space Research and Technology Centre (ESTEC), Keplerlaan 1, 2201 AZ Noordwijk, The Netherlands
[36] Department of Astronomy, Graduate School of Science, The University of Tokyo, 7-3-1 Hongo, Bunkyo-ku, Tokyo 113-0033, Japan
[37] Howard Community College, 10901 Little Patuxent Pkwy, Columbia, MD 21044, USA
[38] Observatoire du Mont-Mégantic, Université de Montréal, Montréal, QC H3C 3J7, Canada
[39] Department of Physics and Astronomy, University of New Mexico, 1919 Lomas Boulevard NE, Albuquerque, NM 87131, USA
[40] School of Physics & Astronomy, University of Birmingham, Edgbaston, Birmingham, B15 2TT, UK
[41] Kavli Institute for Astrophysics and Space Research, Massachusetts Institute of Technology, Cambridge, MA 02139, USA
[42] El Sauce Observatory, Coquimbo Province, Chile
[43] Komaba Institute for Science, The University of Tokyo, 3-8-1 Komaba, Meguro, Tokyo 153-8902, Japan

[44] Department of Astronomy and Tsinghua Centre for Astrophysics, Tsinghua University, Beijing 100084, People's Republic of China
[45] Astrobiology Research Unit, Université de Liège, 19C Allèe du 6 Août, B-4000 Liège, Belgium
[46] Grand Pra Observatory, Switzerland
[47] Observatori Astronòmic Albanyà, Camí de Bassegoda S/N, Albanyà E-17733, Girona, Spain
[48] Department of Astronomy, Wellesley College, Wellesley, MA 02481, USA
[49] Okayama Observatory, Kyoto University, 3037-5 Honjo, Kamogatacho, Asakuchi, Okayama 719-0232, Japan
[50] Department of Multi-Disciplinary Sciences, Graduate School of Arts and Sciences, The University of Tokyo, 3-8-1 Komaba, Meguro, Tokyo 153-8902, Japan
[51] Space Sciences, Technologies and Astrophysics Research (STAR), Institute, Université de Liège, 19C Allée du 6 Août, B-4000 Liège, Belgium
[52] Dept. of Physics & Astronomy, Swarthmore College, Swarthmore, PA 19081, USA
[53] Department of Astronomy, Ohio State University, 140 West 18th Avenue, Columbus, OH 43210, USA
[54] Department of Physics and Astronomy, University of Louisville, Louisville, KY 40292, USA
[55] Société Astronomique de France, 3 Rue Beethoven, F-75016 Paris, France
[56] The Maury Lewin Astronomical Observatory, Glendora, CA 91741, USA
[57] Campo Catino Astronomical Observatory, Regione Lazio, Guarcino (FR), I-03010, Italy
[58] Villa '39 Observatory, Landers, CA 92285, USA
[59] Department of Physics and Astronomy, University of New Mexico, 210 Yale Boulevard NE, Albuquerque, NM 87106, USA
[60] Private Astronomical Observatory, Nezavisimosti 114g, Ananjev, Odessa region, 66400, Ukraine
[61] Department of Astronomy, University of Tokyo, 7-3-1 Hongo, Bunkyo-ku, Tokyo 113-0033, Japan
[62] Astrobiology Center, 2-21-1 Osawa, Mitaka-shi, Tokyo 181-8588, Japan
[63] National Astronomical Observatory, 2-21-1 Osawa, Mitaka-shi, Tokyo 181-8588, Japan
[64] Instituto de Astrofísica de Canarias (IAC), E-38205 La Laguna, Tenerife, Spain
[65] Departamento de Astrofísica, Universidad de La Laguna (ULL), E-38206 La Laguna, Tenerife, Spain
[66] JST, PRESTO, 3-8-1 Komaba, Meguro, Tokyo 153-8902, Japan
[67] National Astronomical Observatory of Japan, 2-21-1 Osawa, Mitaka, Tokyo 181-8588, Japan
[68] Instituto de Astrofisica de Canarias (IAC), 38205 La Laguna, Tenerife, Spain
[69] Observatory Montcabrerm MPC 213 Cabrils, Barcelona, Spain
[70] AAVSO, 5 Inverness Way, Hillsborough, CA 94010, USA
[71] NCCR/PlanetS, Centre for Space & Habitability, University of Bern, Bern, Switzerland
[72] Instituto de Astrofísica de Canarias (IAC), E-38205 La Laguna, Tenerife, Spain
[73] Departamento de Astrofísica, Universidad de La Laguna (ULL), E-38206, La Laguna, Tenerife, Spain
[74] Space Sciences, Technologies and Astrophysics Research (STAR) Institute, Université de Liège, 19C Allée du 6 Août, B-4000 Liège, Belgium
[75] Departamento de Matemática y Física Aplicadas, Facultad de Ingeniería, Universidad Católica de la Santísima Concepción, Alonso de Rivera 2850, Concepción, Chile
[76] NASA Goddard Space Flight Center, 8800 Greenbelt Rd, Greenbelt, MD 20771, USA
[77] Patashnick Voorheesville Observatory, Voorheesville, NY 12186, USA
[78] RASC Calgary Alberta, Calgary, AB T2P 4J3, Canada
[79] Kotizarovci Observatory, Sarsoni 90, 51216 Viskovo, Croatia
[80] Hazelwood Observatory, Australia
[81] Perth Exoplanet Survey Telescope, Perth, Australia
[82] Curtin Institute of Radio Astronomy, Curtin University, Bentley, 6102, Australia
[83] Institute of Astronomy and Astrophysics, Academia Sinica, P.O. Box 23-141, Taipei 10617, Taiwan, R.O.C.
[84] Department of Astrophysics, National Taiwan University, Taipei 10617, Taiwan, R.O.C.
[85] Department of Astrophysical and Planetary Sciences, University of Colorado, Boulder, CO 80309, USA
[86] Tsinghua International School, Beijing 100084, People's Republic of China
[87] Stanford Online High School, 415 Broadway Academy Hall, Floor 2, 8853, Redwood City, CA 94063, USA
[88] Mt. Stuart Observatory, New Zealand
[89] Department of Physics, Engineering and Astronomy, Stephen F. Austin State University, 1936 North Street, Nacogdoches, TX 75962, USA

Abstract

Astronomers do not have a complete picture of the effects of wide-binary companions (semimajor axes greater than 100 au) on the formation and evolution of exoplanets. We investigate these effects using new data from Gaia Early Data Release 3 and the Transiting Exoplanet Survey Satellite mission to characterize wide-binary systems with transiting exoplanets. We identify a sample of 67 systems of transiting exoplanet candidates (with well-determined, edge-on orbital inclinations) that reside in wide visual binary systems. We derive limits on orbital parameters for the wide-binary systems and measure the minimum difference in orbital inclination between the binary and planet orbits. We determine that there is statistically significant difference in the inclination distribution of wide-binary systems with transiting planets compared to a control sample, with the probability that the two distributions are the same being 0.0037. This implies that there is an overabundance of planets in binary systems whose orbits are aligned with those of the binary. The overabundance of aligned systems appears to primarily have semimajor axes less than 700 au. We investigate some effects that could cause the alignment and conclude that a torque caused by a misaligned binary companion on the protoplanetary disk is the most promising explanation.

---

[90] 51 Pegasi b Fellow.
[91] NSF Graduate Research Fellow.
[92] Citizen Scientist.

1. Introduction

Many stars in our galaxy reside in binary systems (Fischer & Marcy 1992; Frankowski et al. 2007; Raghavan et al. 2010). These binary systems have semimajor axes ranging from less than 0.01 au (Dimitrov & Kjurkchieva 2010) to greater than 20,000 au (Latham et al. 1991; Jiménez-Esteban et al. 2019). The extreme range in semimajor axes exhibited by binary systems makes it very challenging for any one formation mechanism to explain all observed systems; instead, there are likely multiple pathways by which binary stars may form.

At close separations, binary stars with semimajor axes less than about 100 au may form by disk fragmentation (Adams et al. 1989) and turbulent fragmentation at larger separations followed by migration (Bate 2018). In disk fragmentation, instabilities in massive circumstellar disks collapse and form a second star orbiting in the plane of the disk. At larger separations, binary stars can form through turbulent fragmentation, where turbulence in the initial core leads to fragmentation of the core into an eventual wide-binary system (Offner et al. 2010, 2016; Bate 2018). These binaries can in turn migrate to smaller separations; thus, close binaries form through a mixture of disk and turbulent fragmentation. Another viable mechanism for the formation of wide binaries is core capture, in which initially unbounded stars form, for example, via the dissolution of open clusters (Kouwenhoven et al. 2010) or from pre-stellar core capture (Tokovinin 2017).

Many binary stars are known to host exoplanets (Mugrauer 2019). While some exoplanets orbit around *both* stars in the binary (the so-called circumbinary system; e.g., Doyle et al. 2011), most exoplanets in binary systems orbit closely around just one of the binary components (a circumstellar orbit). In wide-binary systems, it is believed that virtually all planets will be on circumstellar orbits. The effects of a wide-binary companion on a planetary system are debated. Theoretical work has shown that the dynamical influence of wide-binary companions can eject planets and increase the eccentricity of planetary orbits (Kaib et al. 2013; Correa-Otto & Gil-Hutton 2017; Bazsó & Pilat-Lohinger 2020). Binary companions can affect planetary orbits via the Lidov–Kozai mechanism (von Zeipel 1910; Kozai 1962; Lidov 1962), potentially causing tidal migration of planets to tighter orbits. This mechanism could provide an explanation for the existence of hot Jupiters (Wu & Murray 2003; Fabrycky & Tremaine 2007; Petrovich 2015; Dawson & Johnson 2018; Li et al. 2020), although this is not the only mechanism that can explain hot Jupiter orbits (Lin et al. 1996; Batygin et al. 2016; Ngo et al. 2016), and at least some hot Jupiters could not have formed in this way (e.g., Becker et al. 2015, 2017; Weiss et al. 2017; Cañas et al. 2019; Huang et al. 2020). The presence of a torque from the binary companion could also misalign the protostellar disk (Batygin 2012; Lai 2014; Hjorth et al. 2021).

On the observational front, statistical analyses have shown that while wide-binary companions with semimajor axes $\gtrsim 1000$ au do not seem to have a significant impact on planet occurrence (Deacon et al. 2016), closer binary companions (of semimajor axes $\lesssim 100$ au) seem to suppress planet occurrence (Kraus et al. 2016; Ziegler et al. 2021), possibly by disrupting the protoplanetary disk (Duchêne 2010).

So far, most observational studies of binary companions to exoplanet hosts have focused on the effects of binary companions as a function of the projected separation, partly due to the difficulty of determining the true separation or orbital elements of binary systems. Traditionally, measuring visual binary-star orbits requires repeated precise observations of the positions of the two stars over years, decades, or even centuries (Mason et al. 2001). However, recently the extremely precise astrometry from ESA's Gaia mission (Gaia Collaboration et al. 2016) has made it possible to derive loose constraints on the orbital elements of visual binary stars using only the masses and instantaneous relative velocities of the two components (Newton et al. 2019; Pearce et al. 2020).

Meanwhile, the advent of exoplanet-detecting space telescopes—specifically, the Kepler mission (Koch et al. 2010) and the Transiting Exoplanet Survey Satellite (TESS; Ricker et al. 2015) that use the transit method to detect exoplanets—have resulted in an explosion in the numbers of planets known in visual binaries. Because the planets discovered by Kepler and TESS transit their host stars, we know that the planetary orbital planes are aligned to within a few degrees of our line of sight.

In this paper, we take advantage of these new observations to study whether there is a tendency toward alignment in the orientation of the orbits of visual binary systems and the orbits of planets that reside in these systems. In particular, we measure the orbital inclination of a sample of visual binary stars in which one component is known to host a transiting exoplanet candidate.

It is important to note that we refer to alignment as the minimum alignment between the binary system orbit and exoplanet orbit, not the stellar rotation axis of the primary star and orbit of the exoplanet as is commonly measured using the Rossiter–McLaughlin effect. We make no assumptions on the orientation of the stellar rotation axis in our analysis.

Because the orbital inclinations of the transiting planets must be close to 90°, an overabundance of edge-on binary orbits implies a preferential alignment between the binary systems and their planets. The observed misalignment is really the minimum possible misalignment of the binary system. If Ω_p, Ω_b, i_p, and i_b are the longitude of the ascending node and the inclination of the planet and binary, respectively, then the misalignment, Δ, between the binary and planet can be expressed as

$$\cos(\Delta) = \cos(i_p)\cos(i_b) + \sin(i_p)\sin(i_b)\cos(\Omega_p - \Omega_b). \quad (1)$$

Since $i_p = 90°$,

$$\cos(\Delta) = \cos(90 - i_b)\cos(\Omega_p - \Omega_b). \quad (2)$$

Thus the observed misalignment $|90 - i_b|$ is only equivalent to the actual misalignment Δ if the longitude of the ascending nodes of the binary system and planet happen to be the same; otherwise, Δ is equivalent to the minimum misalignment between the binary system and planet. A large observed relative inclination means a system is misaligned, while a system with small observed relative inclination could be aligned or misaligned depending on the relative (unknown) longitude of the ascending nodes of the
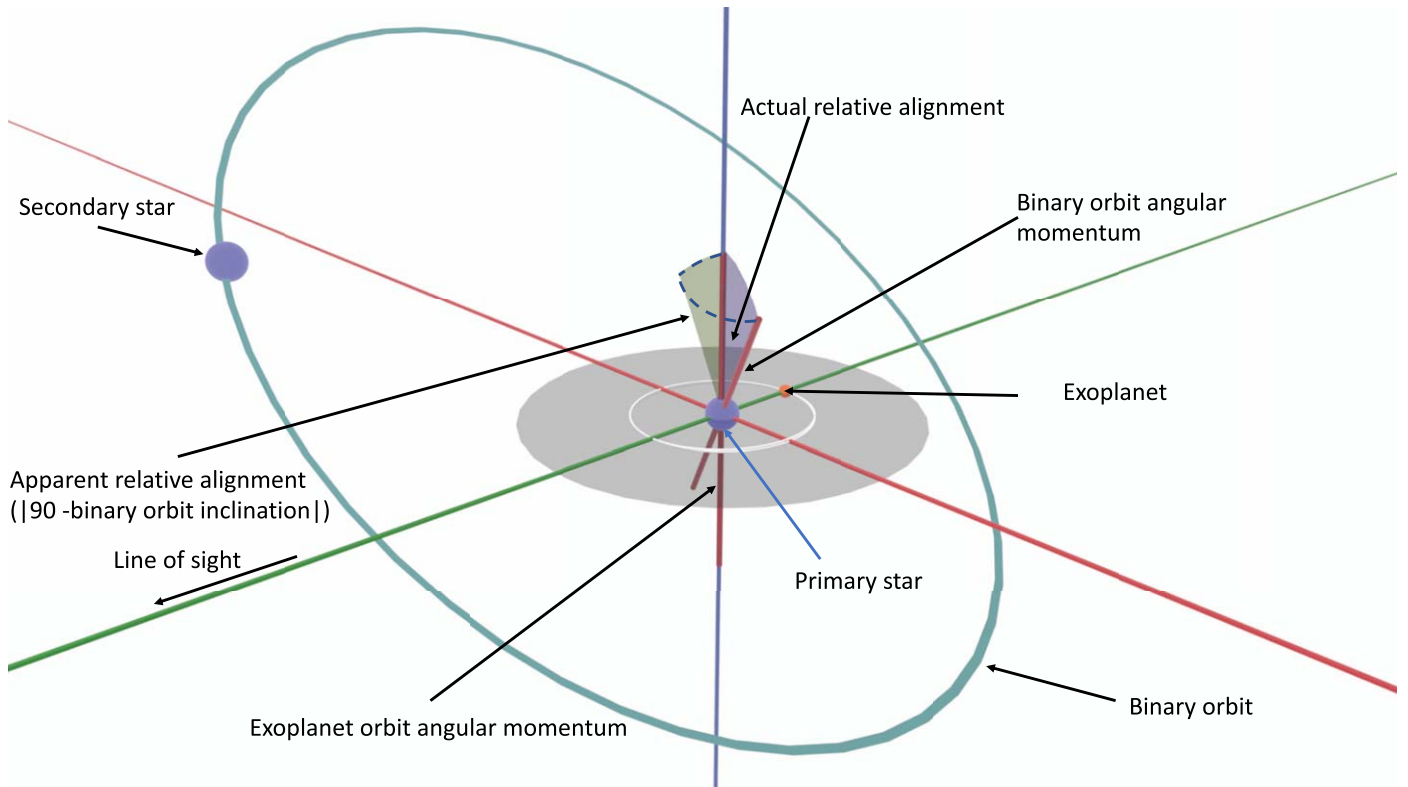
Figure 1. A diagram of the orbital configurations relevant to this paper. The diagram is centered on the primary star. Apparent relative alignment is calculated as $|90° - i|$, where i is the inclination of the binary system (the transiting exoplanets will always have approximately 90° inclination). In the diagram, the green wedge is the inclination of the binary system. The primary star is the star that hosts the exoplanet, while the binary companion is the companion star without detected exoplanets. The angular momentum of the star is the axis that the star rotates on. The exoplanet (orange) orbits at 90° to the line of sight.

exoplanet and binary orbit. However, if many systems are observed, an overabundance of small relative inclinations has the physical interpretation that an overabundance of systems tends to be aligned since the longitude of the ascending nodes of misaligned systems is expected to be distributed randomly and independently of relative inclination. A diagram of the relevant parameters described in this paper is presented in Figure 1.

This paper is organized as follows. In Section 2 we present the Gaia Early Data Release 3 (EDR3), TESS, and ground-based spectroscopic and photometric observations used in our study. In Section 3 we describe the procedure we use to constrain the masses of the binary systems and subsequently model the orbits of the binary systems. In Section 4, we describe the statistical tests performed on the data and rule out possible biases. Section 5 gives an analysis of two theoretical mechanisms that could possibly cause the observed alignment. In Section 6 we discuss two possible scenarios for the observed alignment and discuss future directions for our work. Finally, in Section 7 we summarize our results.

2. Observations/Data

To investigate whether there is a tendency toward alignment between the orbits of visual binary stars and their planetary systems, we need both a sample of likely transiting planet candidates and a constraint on the orbital inclinations of any visual binary companions to these planet host stars. For the former, we make use of planet candidates discovered by the TESS mission and vetted with ground-based follow-up photometric and spectroscopic observations. For the latter, we use astrometric observations from Gaia, archival broadband photometry, and metallicity

measurements from both new and archival spectra to determine the masses of the binary components using isochrone fitting. We also perform a variety of cuts on our sample of visual binaries with exoplanets and a control sample. A diagram of the various cuts performed is shown in Figure 2. We describe these inputs to our analysis and the cuts we performed in more detail in this section.

2.1. TESS Planet Candidates

2.1.1. Identification with TESS

We start with the list of planet candidates reported by the TESS mission (also known as TESS Objects of Interest, or TOIs). TESS uses four 10 cm cameras to repeatedly image 96° by 24° regions of the sky for 28 days at a time. After the completion of each 28 day observation (called a sector), TESS moves to a new field of view and repeats the process. Over the course of its 2 year primary mission, TESS observed approximately 70% of the sky, and is continuing to observe in an extended mission.

The TESS CCDs read out images of the sky every 2 s, but the data volume required to download each 2 s image from orbit would be prohibitively large. Instead, TESS coadds the 2 s images into longer observations before beaming the data back to Earth. Most of the sky is coadded to long-cadence Full Frame Images (FFIs) with exposure times of 30 minutes (in the primary mission) or 10 minutes (in the extended mission), while the pixels surrounding 20,000 preselected stars are coadded to 2 minutes; for the extended mission, 1000 of these targets are coadded to 20 s.
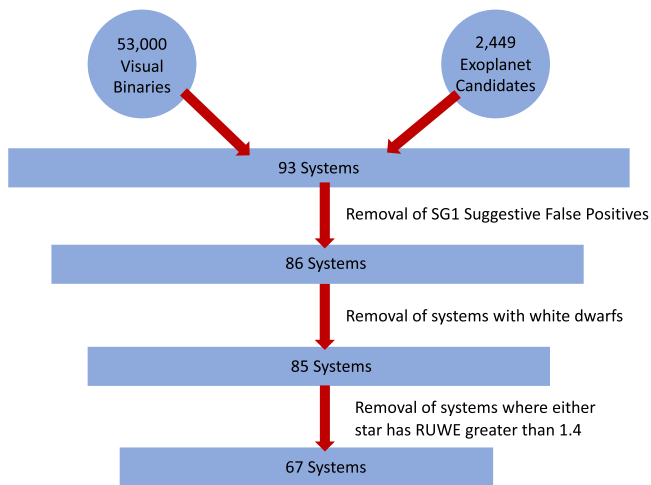
Figure 2. A hierarchy of the cuts performed on the sample of visual binaries with transiting exoplanet candidates. The same cuts were performed on the control sample. The specific cuts performed are described in detail in Section 2.

Once the data have been received on Earth, they are analyzed as described by Guerrero et al. (2021) to process the observations and identify planet candidates. We base our sample on the list of all TESS planet candidates that had been reported online as of 2020 December 15.

2.1.2. Sample of Visual Binaries with Planet Candidates

We identify planet-candidate-hosting stars that also happen to reside in a visual binary system matching the underlying Gaia DR2 ID of items in the TESS Input Catalog (TIC) to a catalog of visual binary stars identified in Gaia data by El-Badry & Rix (2018). This work reports approximately 53,000 visual binary systems within 200 pc of the Sun and with projected separations between 50 and 50,000 au derived from Gaia DR2 astrometric observations. Although the catalog has binaries with separations as small as 50 au, the vast majority of binaries in the catalog have much wider separations. At wider separations, it is more likely that the Gaia spacecraft will resolve the individual stars in the binary system. In total, after all cuts were performed, we identified a sample of 67 visual binary systems including a TESS planet-candidate host star with projected semimajor axes ranging from 61 to 34,700 au and parallaxes ranging from 5 to 48 mas.

2.1.3. Follow-up Ground-based Time-series Photometry

We identified and removed additional false-positive planet candidates using ground-based observations. The majority of these observations came from Sub-Group 1 (SG1) of the TESS Follow-up Observing Program Working Group (TFOP WG), which performs seeing-limited time-series photometry of TOIs. The specific facilities used for follow-up observations are listed in Table 1. SG1 observations have the primary purposes of ruling out the possibility of nearby eclipsing binaries (NEBs) as the source of the TESS detection and refining the parameters of transiting planet candidates.

SG1 observations are used to classify TOIs into a variety of photometric dispositions, indicating whether a given candidate is a false positive, a plausible candidate, or a well-vetted likely planet. The dispositions used by SG1 are as follows:

1. PC, or Planet Candidate, indicates that either no follow-up observations have been conducted, or that they are in progress.
2. PPC, or Promising Planet Candidate, indicates that follow-up observations have ruled out NEB false-positive scenarios on most stars in the field.
3. CPC, or Cleared Planet Candidate, indicates that follow-up observations have ruled out NEB false-positive scenarios on all stars in the field.
4. VPC, or Validated Planet Candidate, indicates that ground-based follow-up observations have detected the transit signal discovered by TESS, confirming that the signal is on-target and not a false alarm.
5. KP, or Known Planet, indicates the candidate was previously identified and confirmed as a planet independently of TESS.
6. LEPC, or Lost Ephemeris Planet Candidate, indicates that the uncertainty on predicted future transit times has grown large enough that ground-based photometric observations cannot efficiently screen for false positives.
7. STPC, or Single Transit Planet Candidate, indicates that the orbital period of the planet is not known and therefore ground-based photometric observations cannot efficiently screen for false positives.
8. NEB, or Nearby Eclipsing Binary, indicates the detection of a NEB that is contaminating the TESS aperture.
9. PNEB indicates a Possible NEB.
10. NPC, or Nearby Planet Candidate, indicates that the TESS detection was actually of a nearby star, but the TESS detection itself is not ruled out to be a false positive. However, the original TOI is retired as a false positive in this case.
11. APC, or Ambiguous Planet Candidate, indicates that results are ambiguous, but suggest that confirming a planet candidate in the system would be difficult.
12. BEB, or Blended Eclipsing Binary, and EB, Eclipsing Binary, indicate the presence of an eclipsing binary as the cause for the TESS detection.
13. FA, or False Alarm, indicates an instrumental anomaly as the cause of the detection.

In this analysis, we consider any TOI with a photometric disposition of PNEB, NEB, NPC, APC, BEB, EB, and FA to be a false positive and remove them from our sample. After this false-positive cut, there are 86 binary systems with exoplanets.

2.2. Visual Binaries from Gaia

2.2.1. Control Sample of Visual Binaries without Planet Candidates

We also identified a control sample of visual binary systems from the El-Badry & Rix (2018) catalog. Kepler has taught us that most of these stars likely host planetary systems of their own (e.g., Fressin et al. 2013; Deacon et al. 2016), but since they do not host any transiting planets, their inclinations will be unknown. Therefore, performing our analysis on a control sample and comparing the results against the sample of binaries with planet candidates helps give us confidence that any features we see in the resulting distribution of inclination angles are astrophysical and not due to selection effects. We specifically constructed our control sample to have nearly identical properties to the sample of binaries with planet candidates to make sure that our control sample incorporates any selection biases from the TESS planet-detection process.

Observatory/Telescope	Location	Aperture (m)	Pixel Scale (arcsec)	FOV (arcmin^2)
Acton Sky Portal (Private Observatory)	Acton, MA, USA	0.36	0.69	17.3 × 11.5
Adams Observatory at Austin College	Sherman, TX, USA	0.61	0.38	26 × 26
Antarctic Search for Transiting ExoPlanets (ASTEP)	Concordia Station, Antarctica	0.4	0.93	63 × 63
Chilean-Hungarian Automated Telescope (CHAT)	Las Campanas Observatory, Chile	0.7	0.6	21 × 21
Deep Sky West	Rowe, NM, USA	0.5	1.09	37 × 37
El Sauce Observatory (Evans Private Telescope)	Coquimbo, Chile	0.36	1.47	19 × 13
Fred L. Whipple Observatory (FLWO)	Amado, Arizona, USA	1.2	0.672	23.1 × 23.1
George Mason University (GMU)	Fairfax, Virginia, USA	0.8	0.35	23 × 23
Grand-Pra Observatory	Valais Sion, Switzerland	0.4	0.73	12.9 × 12.55
Hazelwood Private Observatory	Churchill, Victoria, Australia	0.32	0.55	20 × 14
Infrared Survey Facility (IRSF/SIRIUS)	South Africa	1.4	0.45	7.7 × 7.7
Las Cumbres Observatory Global Telescope (0.4 m)	Spain, Australia	0.4	0.571	29.2 × 19.5
Las Cumbres Observatory Global Telescope (1 m)	Chile, South Africa, Australia, USA	1.0	0.39	26 × 26
Las Cumbres Observatory Global Telescope (2 m/MuSCAT3)	Haleakala, Hawaii, USA	2.0	0.27	9.5 × 9.5
MEarth-South Observatory	La Serena, Chile	0.4	0.84	29 × 29
Mt. Kent Observatory (CDK700)	Toowoomba, Australia	0.7	0.4	27 × 27
Mt. Stuart Observatory	Dunedin, New Zealand	0.3175	0.88	44 × 30
Mt. Lemmon Observatory	Tucson, AZ, USA	0.61	0.39	26 × 26
Observatoire du Mont-Mégantic (OMM)	Notre-Dame-des-Bois, Québec, Canada	1.6	0.47	7.95 × 7.95
Observatori Astronòmic Albanyà (OAA)	Albanyà, Girona, Spain	0.406	1.44	36 × 36
Okayama 188 cm Telescope (MuSCAT)	Okayama, Japan	1.88	0.358	6.1 × 6.1
Perth Exoplanet Survey Telescope (PEST)	Perth, Australia	0.3	1.2	31 × 21
Kotizarovci Observatory	Sarsoni, Croatia	0.3	1.21	15 × 10
Private observatory of the Mount	Saint-Pierre-du-Mont, France	0.20	0.69	38 × 29
Sierra Nevada Observatory	Granada, Andalucía, Spain	1.5	0.232	7.92 × 7.92
Teide Observatory (MuSCAT2)	La Laguna, Spain	1.52	0.44	7.4 × 7.4
TRAPPIST-North	Oukaimeden Observatory, Morocco	0.6	0.64	22 × 22
Virtual Telescope Project	Ceccano, Italy	0.43	1.2	16 × 11
Whitin Observatory at Wellesley College	Wellesley, MA USA	0.7	0.67	23 × 23

To achieve this goal, we defined a metric, $\mathcal{M}$, to quantify the similarity between any two visual binary systems:

$$\mathcal{M} = \left(\frac{\Delta G_1}{4}\right)^2 + \left(\frac{\Delta G_2}{4}\right)^2 + \left(\frac{\Delta RP_1}{4}\right)^2 + \left(\frac{\Delta RP_2}{4}\right)^2$$
$$+ \left(\frac{\Delta BP_1}{4}\right)^2 + \left(\frac{\Delta BP_2}{4}\right)^2 + (\Delta \varpi)^2 + (\Delta s)^2, \quad (3)$$

where s is the projected separation of the two stars in the binary system, ϖ the system parallax, and G, BP and RP are the stars' apparent magnitudes in the three Gaia passbands. Here, the Δ symbol represents the normalized fractional difference between the values for the two systems: a system with a transiting exoplanet and potential control sample system, and the subscripts 1 and 2 represent the primary and secondary star in each system. For instance, $\Delta G_1 = \frac{(G_1 - G_c)}{G_c}$, where c represents the control sample. We arbitrarily divide all magnitude normalized differences by 4 so that not all weight is given to the magnitudes.

For each of the visual binary systems with non-false-positive exoplanets as of 2020 December 25, we identified the 12 systems from the El-Badry & Rix (2018) catalog with the lowest $\mathcal{M}$ metric. Systems were not removed after each sampling procedure (i.e., they are allowed to be included twice); however, due to the large number of systems present in the El-Badry & Rix (2018) catalog, the resulting control sample has no repeated systems. A subset of our planet-candidate sample was also identified by El-Badry & Rix (2019) to have spectroscopic metallicity measurements from one of several

large spectroscopic surveys (see Section 2.3.1). For these systems, we restricted our search for similar systems to those that also have an archival spectroscopic metallicity measurement from El-Badry & Rix (2019). In total, we identify a control sample of 960 systems with very similar distributions of parameters to the input sample of binaries containing planet candidates. Figure 3 shows various properties of the sample with exoplanets and control sample.

2.2.2. Astrometric Parameters

Our analysis hinges on highly precise measurements of the positions, proper motions, and parallaxes of each star in the visual binary system. Originally we used parameters from Gaia Data Release 2 (DR2; Gaia Collaboration et al. 2018; Lindegren et al. 2018), which were based on 22 months of data. During the preparation of our manuscript, updated astrometric parameters based on 34 months of data became available in Gaia EDR3 (Gaia Collaboration et al. 2021; Lindegren et al. 2021). We performed our full analysis using data from both Gaia DR2 and EDR3 and found consistent results between the two samples. We present the results from our analysis using the more precise Gaia EDR3 data in the rest of this paper.

2.2.3. Removing Incorrect Cross-matches, High-RUWE Solutions, and White Dwarfs

We apply a variety of cuts to both the control sample and sample with exoplanets in order to ensure that only high-quality astrometric parameters are preserved.
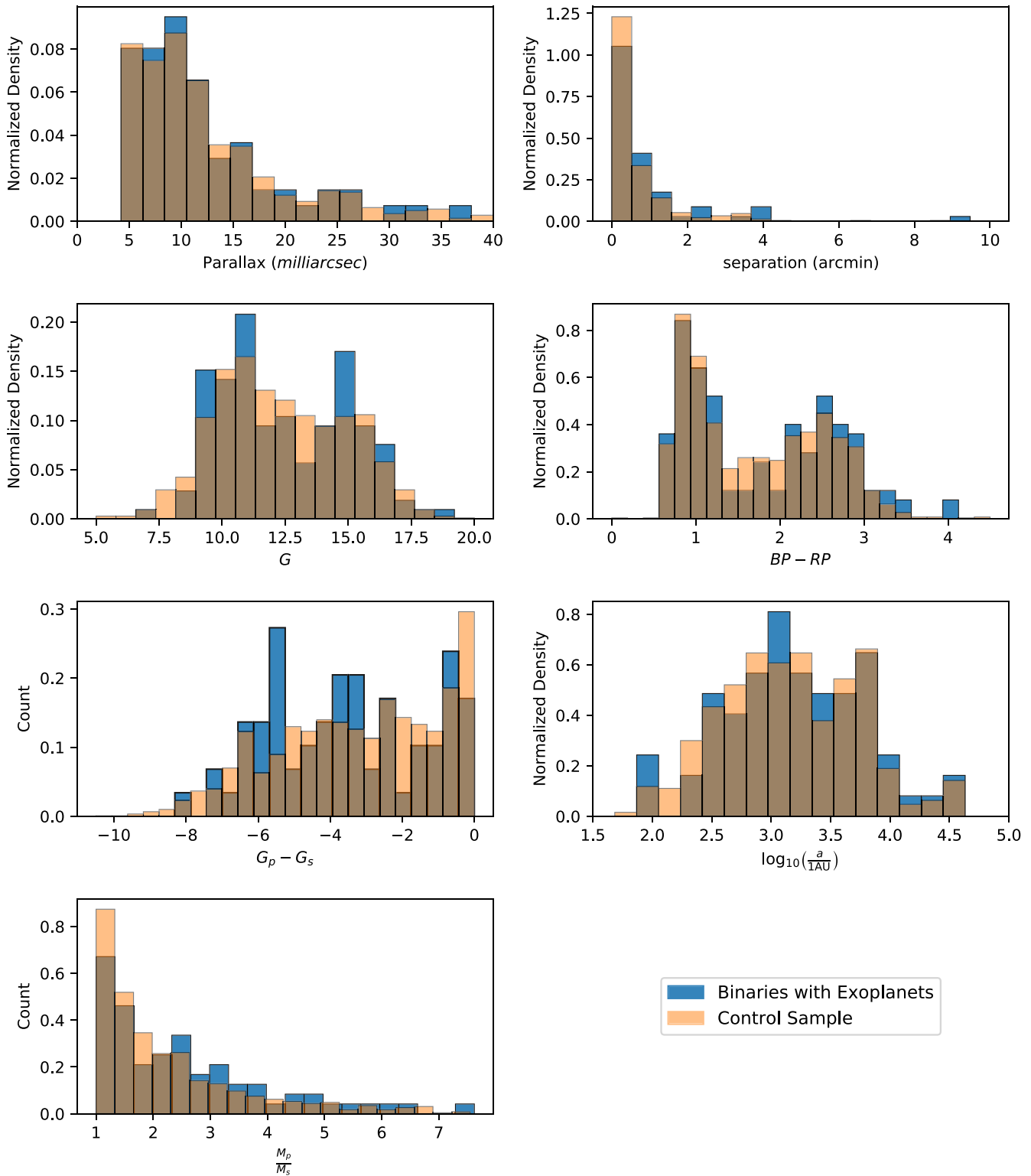
Figure 3. Histograms of properties of the binary systems. From left to right: parallax in milliarcseconds, projected separation in arcminutes, apparent G magnitude, $BP - RP$ color, $G_p - G_s$, where p is the primary star (defined as the brighter star) and s is the secondary star, $\log_{10}(a)$ where a is the projected semimajor axis, and mass ratio of the primary and secondary star.

In the process of converting between Gaia DR2 and Gaia EDR3 IDs, a purely positional cross-match can contaminate the sample due to proper motion movement from the Gaia DR2 epoch (2015.5) to the Gaia EDR3 epoch (2016) and the addition of new sources in EDR3. To ensure that there are no incorrectly cross-matched stars in our sample, we exclude 17 binary systems in the control sample for which $|G_{\mathrm{EDR3}} - G_{\mathrm{DR2}}| > 0.05$.

The renormalized unit weight error (RUWE) can be used as an indicator of the quality of the Gaia astrometric solution for a star (Lindegren 2018). The RUWE is the square root of the

reduced χ^2 divided by a correction function that eliminates dependence on G magnitude and $BP - RP$ color. An RUWE of greater than 1.4 typically indicates a poor astrometric fit, so we eliminate any systems for which the RUWE for at least one of the stars is greater than 1.4. A high RUWE can indicate the presence of an unresolved companion (Belokurov et al. 2020).

We also remove any binaries where either the host star or companion star is a white dwarf; it is more difficult to estimate masses for white dwarfs than for main-sequence stars, and in these systems the binary orbit has been influenced by post-main-sequence mass loss. While these effects are very interesting in their own right, it is beyond the scope of this work to consider them.

After these cuts, there are 67 binary systems with exoplanets and 688 binary systems in the control sample. The distribution of the radii and the periods of the exoplanets in our sample are shown in Figure 4.

2.2.4. Other Work Identifying Visual Binaries in Gaia

The El-Badry & Rix (2018) catalog we used in this study is not the only list of visual binary stars including planet candidates. Recently, Mugrauer & Michel (2020) presented a sample of 193 binary companions of TESS exoplanets. Although Mugrauer & Michel (2020) identify a significantly larger number of possible binary companions to TOIs, they do not identify visual binaries in non-planet-hosting stars with the same criteria that we could use to construct a control sample, so we cannot include these additional binaries in our analysis. Ziegler et al. (2020) used speckle imaging with the Southern Astrophysical Research Observatory to search for binary companions to TOIs. They then compared their discovered companions to those discovered in Gaia DR2. Many of their systems overlap with our sample.

During the final preparation of our manuscript, El-Badry et al. (2021) reported an updated search for visual binaries using the more precise astrometric parameters from Gaia EDR3, including a significant increase in the number of identified systems. In the future, we could perform the same analysis in this paper on their larger sample of visual binaries and potentially increase the statistical significance of our results. We checked and found that most of the binary systems (92%) in our sample lie in the sample of El-Badry et al. (2021), with the inclination distribution being virtually the same when excluding those systems not in El-Badry et al. (2021).

2.3. Ground-based Spectroscopy

Fitting binary orbits using only instantaneous positions and proper motions from Gaia requires an estimate of the mass of each binary component, which in turn requires an estimate of each star's metallicity. To derive the metallicities of stars in our samples, we use both archival observations from large spectroscopic surveys and targeted follow-up observations of planet-candidate host stars made by the TESS Follow-up Observing Program (TFOP). Below, we describe the sources of our spectroscopic parameters and the procedure we used to determine the metallicities of the observed stars. Because the components of relatively wide-binary stars are known to have nearly identical elemental abundances in most cases (Hawkins et al. 2020), we assume the metallicity of both stars in the binary are the same when we only have metallicity measurements for one of the pair.

(a)

(b)
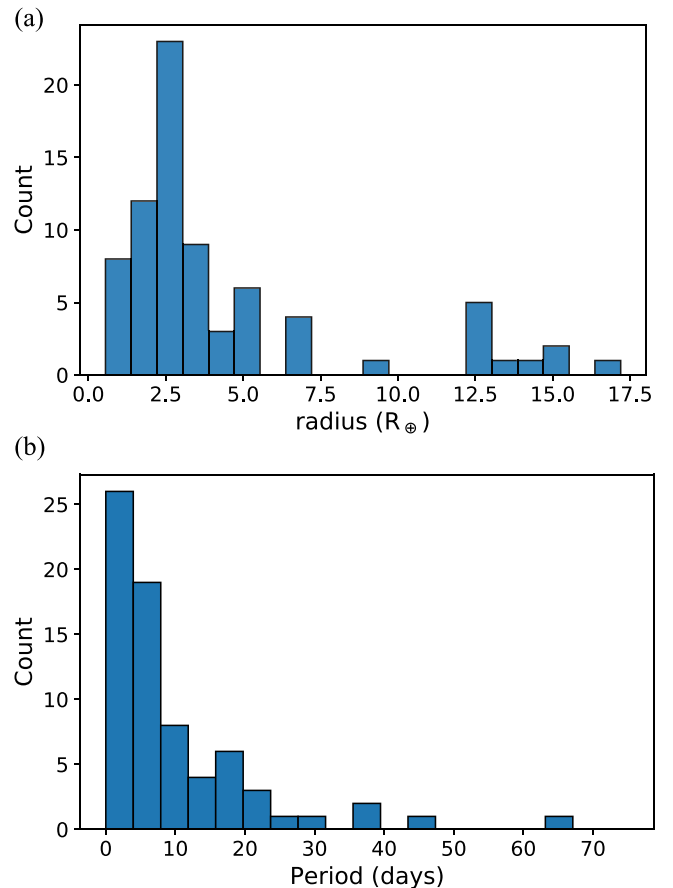
Figure 4. Most of the planets in our sample are small (1–5 $R_\oplus$), and thus have relatively low false-positive probabilities (e.g., Morton & Johnson 2011; Guerrero et al. 2021) compared to giant planet candidates (Santerne et al. 2012).

For stars that have more than one spectroscopic observation, we use an average of the metallicities derived from the separate spectroscopic observations and add the errors from each separate observation in quadrature.

2.3.1. Archival Spectroscopy

Many of the stars in our samples have archival spectra and published metallicity estimates. El-Badry & Rix (2019) cross-matched their sample of visual binary stars (El-Badry & Rix 2018) with stars observed by large spectroscopic surveys and identify a subset of 8507 binaries for which spectroscopic metallicities have been reported in the literature for at least one component. The archival metallicities they identify come from the following surveys or compilations: RAVE (Steinmetz 2003; Kunder et al. 2017), LAMOST (Zhao et al. 2012), Hypatia (Hinkel et al. 2014), APOGEE (Majewski et al. 2016), and GALAH (Buder et al. 2018; Čotar et al. 2019). Of the stars in our sample of binary stars with planet candidates, 16 stars have a metallicity from RAVE, one from LAMOST, four from the Hypatia catalog, two from APOGEE, and two from GALAH.

2.3.2. Las Cumbres Observatory/Network of Robotic Echelle Spectrographs

We obtained observations of seven stars from our sample of binary stars with planet candidates using the Network of Robotic Echelle Spectrographs (NRES), a set of four identical

optical echelle spectrographs connected to the Las Cumbres Observatory (LCO) global telescope network (Brown et al. 2013; Eastman et al. 2014; Siverd et al. 2017, 2018). Each spectrograph is fiber-fed by one of the 1 m telescopes in the LCO network. NRES achieves a spectral resolution of $R \sim 53{,}000$ over the wavelength range 390–860 nm. We derive stellar parameters from NRES spectra using the SpecMatch algorithm (Petigura 2015; Petigura et al. 2017), which compares the observed spectra to the synthetic spectra of Coelho et al. (2005).

2.3.3. Tillinghast Reflector Echelle Spectrograph

We observed 15 stars with the Tillinghast Reflector Echelle Spectrograph (TRES), an optical echelle spectrograph with a wavelength range of 385–910 nm. TRES is located on the 1.5 m telescope at the Whipple Observatory on Mt. Hopkins in Arizona and has a resolution of $R = 44{,}000$ (Fűrész 2008; Mink 2011). The TRES metallicities are derived using the Stellar Parameter Classification tool (SPC). SPC cross-correlates the observed spectra of stars with a grid of around 51,000 model spectra. The peaks of the cross-correlation function (CCF) are then fitted with a polynomial over four stellar parameters (T_{eff}, $\log(g)$, [Fe/H], $v \sin(i)$) in an attempt to determine the location of the highest point between grid points. If multiple observations are available for a star, the mean metallicity is weighted by the corresponding highest peak of the CCF in the SPC results for each observation (Buchhave et al. 2012, 2014; Buchhave & Latham 2015). For all stars with $T_{eff} < 4500\,K$ (indicating that the star is a cooler, dwarf-like star), a Yale-Yonsei isochrone is used as a prior for the star's $\log(g)$, T_{eff}, and [Fe/H] (Spada et al. 2013); this additional step improves the reliability of spectroscopic parameters for cool stars.

2.3.4. FIbre-fed Echelle Spectrograph

We observed six stars with the FIbre-fed Echelle Spectrograph (FIES). FIES is located on the 2.56 m Nordic Optical Telescope (NOT) in La Palma, Spain (Telting et al. 2014). FIES has three observation modes that offer different spectral resolution and throughput; our observations use the highest resolution ($R = 67{,}000$) $1{\farcs}3$ fiber. Metallicities are derived using SPC in a similar manner to the TRES metallicities.

2.3.5. CTIO High Resolution Spectrometer

We observed eight stars with the CTIO High Resolution spectrometer (CHIRON) located on the 1.5 m SMARTS telescope at the Cerro Tololo Inter-American Observatory in Chile. CHIRON is a fiber-fed optical echelle spectrograph that achieves a resolution of $R \sim 79{,}000$ and a wavelength range of 415–880 nm (Schwab et al. 2010; Tokovinin et al. 2013). Metallicities are derived by interpolating the CHIRON spectra to a sample of around 10,000 TRES spectra with parameters derived by SPC using a gradient-boosting regressor. When multiple CHIRON observations are present for a star, the mean of the observations is used, with error added in quadrature.

3. Analysis

Here, we describe the calculations needed to constrain the inclination angle of each binary orbit in our sample. This involves two main steps: (1) estimating the mass of each star in

the binary system, and (2) given these stellar masses and the Gaia astrometric parameters, determining plausible orbital parameters using the LOFTI software package (Pearce et al. 2020).

3.1. Stellar Mass Determination

We derive masses for the stars in our samples using the Isochrones Python package (Morton 2015). Given observable parameters like a star's apparent magnitudes in different bandpasses, its trigonometric parallax, and spectroscopic parameters, Isochrones determines the star's most likely physical parameters and their uncertainties by comparing measured parameters to those predicted by stellar evolution and atmosphere models. Isochrones supports several different suites of isochrone models; we use the MIST isochrones (Choi et al. 2016; Dotter 2016). We input each star's parallax, metallicity (when available from archival spectroscopy or NRES, TRES, FIES, or CHIRON), and apparent magnitudes in the G, BP, and RP bandpasses from Gaia and the J, H, and K bandpasses from the 2MASS survey (Skrutskie et al. 2006). For uncertainties in bandpasses, we use the error floors of Eastman (2017).

Not all of the stars in our samples have spectroscopic metallicity measurements. If a star does not have a metallicity value, the metallicity of its companion is used (see Hawkins et al. 2020). If neither star in a binary pair has a spectroscopic metallicity measurement, we use the isochrones default metallicity[93], a prior based on a two-Gaussian fit to the distribution of metallicities reported by Casagrande et al. (2011).

Model isochrones are not as well calibrated for M-dwarf stars (which constitute around half of the stars in the sample of visual binaries) as they are for Sun-like stars (Angus et al. 2019). For M dwarfs, we use the $M_K - M_\star$ relationship of Mann et al. (2019) using the accompanying M_-M_K- Python package[94] to estimate the stars' mass. M_k magnitudes, when available, are taken from the TIC (Stassun et al. 2019). Any stars in the range $4.5 < M_k < 10.5$ (the more conservative option given by Mann et al. 2019) are treated as M dwarfs.

Rough mass estimates for these stars are also provided in the TIC (Stassun et al. 2019). We compare our mass estimates to the TIC estimates, as demonstrated for the control sample in Figure 5, to ensure that there are no systematic discrepancies in estimation. The median uncertainty of the masses in our sample is 0.016 $M_\odot$ and in the TIC 0.082 $M_\odot$. We also compare our mass estimations to those derived from spectral energy distribution modeling (Stassun et al. 2018), where stellar atmosphere model grids are interpolated in T_{eff}, $\log g$, and [Fe/H] and combined with spectroscopic $\log g$ measurements. There is general agreement between the masses derived from both techniques, an independent check of the masses assigned to the stars.

3.2. LOFTI Modeling

Linear Orbits for The Impatient (LOFTI; Pearce et al. 2020) uses measurements of the relative positions of two stars (in both R.A., $\Delta\alpha$, and decl., $\Delta\delta$), relative proper motions, relative radial velocity (if available), and stellar masses to constrain orbits of visual binaries. In our analysis, we take all of these
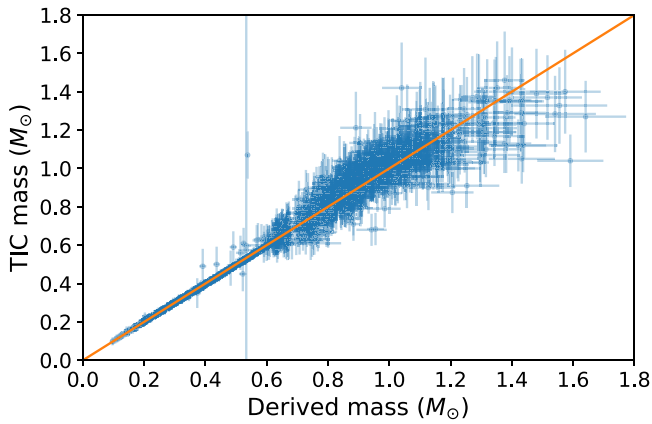

Figure 5. A comparison between the masses derived using isochrone fitting in this paper versus the TIC-derived masses for the control sample. The plotted error bars are one standard deviation. An orange line denotes where a 1:1 correspondence of masses would lie. We see good correspondence between our mass estimates and those in the TIC.

Figure 6. 100 orbits from the posterior of a sample LOFTI fit.

parameters from Gaia. LOFTI calculates relative proper motion and position as primary minus companion, while relative radial velocity is calculated as companion minus primary. LOFTI uses the Orbits for the Impatient (OFTI) sampling and rejection technique (Blunt et al. 2017) applied to Gaia astrometric parameters.

OFTI, on which LOFTI is based, optimizes orbit fitting via rejection sampling with the unique scale and rotate step. The algorithm randomly samples eccentricity (e), argument of periastron (ω), mean anomaly from derived epoch of periastron (t_o), and cosine of inclination ($\cos(i)$) from uniform priors, then scales the semimajor axis (a) and rotates the longitude of the ascending node (Ω) to match the observed separation in binaries, rejecting orbits if the χ^2 probability (proportional to $e^{-\chi^2/2}$) is greater than a randomly chosen number in the range [0, 1] to form a posterior distribution of orbital parameters. OFTI is computationally advantageous over traditional Markov Chain Monte Carlo methods for visual binary systems, where orbital parameters are often poorly constrained (Blunt et al. 2017, 2020). Table 2 is a list of priors used in the LOFTI algorithm on sampled parameters, while Table 3 shows parameters calculated either from sampled parameters or via the scale and rotate method.

Orbital fitting using very short observational baselines (as done here) can lead to degeneracies in parameters. Particularly, for high eccentricity values, inclination is biased toward edge-on orbits (Ferrer-Chávez et al. 2021). The inclusion of a control sample in our study should allow us to determine if there is a preferential alignment regardless of the presence of this bias.

We ran LOFTI on the binary systems with exoplanets and those in the control sample. We continued sampling the posterior distributions until we reached 100,000 accepted orbits. We performed this computationally intensive task on the Maverick 2 and Lonestar 5 supercomputer clusters at the Texas Advanced Computing Center.

We show 100 orbits drawn from a sample LOFTI posterior in Figure 6 and a sample posterior distribution of parameters from LOFTI for one binary system in Appendix A. We also show archival ground-based images of two characteristic systems, one aligned and one misaligned, annotated with astrometric information from Gaia in Figure 7.
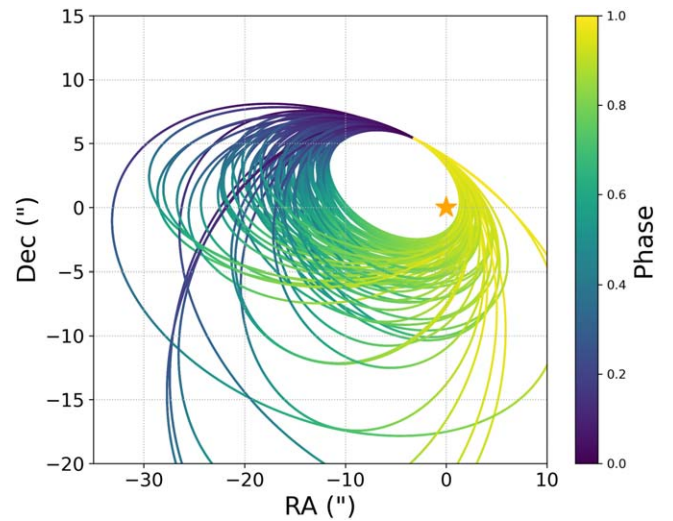
Table 2
List of Priors for Orbital Parameters that are Randomly Sampled in LOFTI

Parameter	Prior
Eccentricity (e)	Uniform(0, 1)
Inclination (i)	Sin(0, 180)
Argument of periastron (w)	Uniform(0, 360)
t_{const}	Uniform(0, 1)
Total mass (M_{tot})	Normal(M_0,M_{std})
Distance	Normal(D_0,D_{std})

Note. t_{const} is a value used in the calculation of the epoch of periastron passage (t_0).

Table 3
List of Orbital Parameters that are Calculated Either from Sampled Parameters or Calculated Using the Scale and Rotate Method to Match Observed Data

Parameter	Formula
Period (T)	$\left(\frac{a^3}{M_{tot}}\right)$
Epoch of periastron passage (t_0)	$d_{epoch} - t_{const} * T$
Semimajor axis a	Scale and rotate
Longirude of ascending node (Ω)	Scale and rotate

Note. d_{epoch} is the date of the epoch of the observations.

4. Results

After obtaining orbital parameters for all of the visual binary systems in our samples, we calculated the difference in median inclination between the plane of each visual binary orbit and the orbit of the planetary system orbiting that same primary. Since the planets in our sample were all detected using the transit method by TESS, they all have inclinations with respect to the plane of the sky very close to 90°. The minimum difference in inclination between the binary-star system and planet can be expressed by $|90° - i|$. We calculate this value for each system in both our sample of binaries containing transiting planet candidates and our control sample of binaries without detected exoplanets to account for selection effects in the El-Badry & Rix (2018) catalog or biases in our orbit fitting (Ferrer-Chávez et al. 2021).
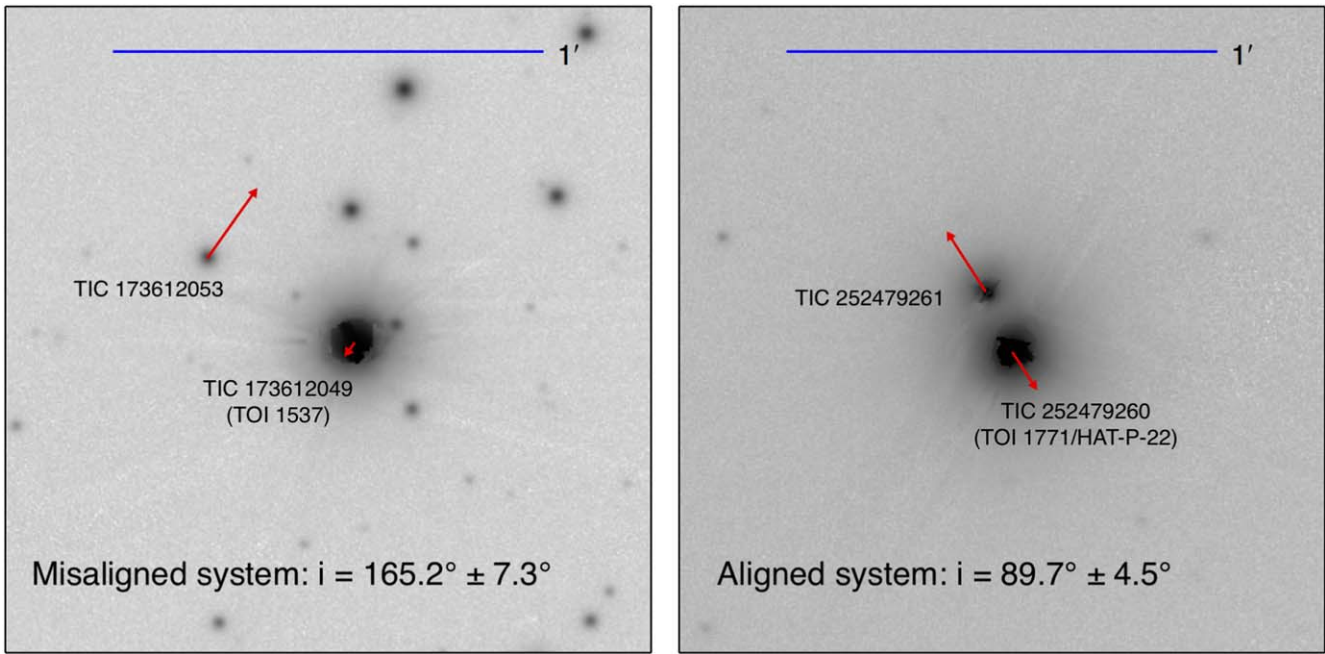
Figure 7. Images from the Pan-STARRS survey (Chambers et al. 2016) of selected binary systems from our sample of transiting exoplanet hosts. In each image, the exoplanet host and its binary companion are labeled (with the planet host labeled as a TOI); red arrows show their relative proper motion after subtracting the velocity of the system's center of mass. The blue bar at the top of each image shows the scale. The two images are labeled with the binary inclination from our LOFTI fits. The image on the left is misaligned with the orbit of the transiting planet, while the image on the right shows an aligned orbit. In general, only orbits with $i = 90$ will have proper motion vectors that are parallel to the projected semimajor axis. All other angles between proper motion vectors and projected semimajor axes a priori allow all inclination values, although given a uniform prior on eccentricity, higher inclination values will be favored for nearly parallel semimajor axis and proper motion vectors.

We show histograms of the median $|90° - i|$ for both our sample of planet candidates and our control sample in Figure 8(a). In Figure 8(b), we show the distribution of $\sin|90 - i|$. If inclination is drawn from an isotropic distribution, $\sin|90 - i|$ should be uniform. There is an apparent overdensity of visual binary systems hosting exoplanets with inclinations close to 90°. Although any given individual system with a binary inclination near 90° might not necessarily be aligned, the overall overdensity suggests a preferential alignment between exoplanet and wide-binary orbit.

The overdensity of well-aligned binary orbits is most apparent at binary separations closer than approximately 700 au. Figure 9 shows the minimum difference in inclination for each system as a function of the binary semimajor axis. Figure 10 shows histograms of $|90° - i|$ for binary systems hosting exoplanets separated by semimajor axis. Evidently, planets are well aligned with the orbits of binary stars with semimajor axes less than about 700 au, while any alignment (if present) between planets and binaries with semimajor axes greater than about 700 au is much weaker. No such dependence in inclination on semimajor axis is seen in the control sample. As can be seen in Figure 9, the 700 au value is very approximate and the actual value could reasonably be much lower or higher due to the small sample sizes we use.

4.1. Kolmogorov–Smirnov Test

We assessed the statistical significance of the apparent alignment between visual binary orbits and their planetary systems using a Kolmogorov–Smirnov (K-S) test. A K-S test measures the maximum difference between the cumulative distributions of two empirical distributions and then calculates a p-value representing the probability that the two empirical distributions were drawn from the same underlying distribution.

A small K-S value indicates that the distributions being compared are not from the same underlying distribution. We perform a K-S test between the sample with exoplanets and control sample's $|90 - i|$ values, where i is the median value of the distribution of inclinations. The test rejects the null hypothesis that the two data sets are drawn from the same underlying distribution with $p = 0.0037$. To check that our significance value is not dependent on our somewhat arbitrary choice of RUWE cutoff, we adjust our RUWE cutoff to 1.3, 1.2 and 1.1, finding that the p-values are, respectively, $p = 0.016$, $p = 0.051$, and $p = 0.045$. Additionally, we use two other statistical tests specifically designed for comparing angular data: Wallraff's nonparametric test (Wallraff 1979) and Watson's nonparametric test (Watson 1983). The Wallraff test yields a p-value of 0.031, while the Watson test yields a p-value in the range [0.001, 0.01] (the test only gives a range of p-values).

None of these tests account for error in the individual measurements of inclination. The K-S test is shown visually as the maximum difference in cumulative distributions in Figure 11.

Since most of the excess of aligned systems are found in binary systems with semimajor axes less than about 700 au, we also compare the distributions of $|90 - i|$ for these close binaries. For systems with semimajor axes less than 700 au compared to the control sample, the K-S test shows stronger evidence that the inclinations in the exoplanet sample and control sample are drawn from different distributions ($p = 0.000250$). Finally, we investigate whether the distributions of inclination above and below 700 au are significantly different from each other. For systems with semimajor axes less than 700 au compared to those with semimajor axes greater than 700 au, the K-S test still shows

(a)

(b)
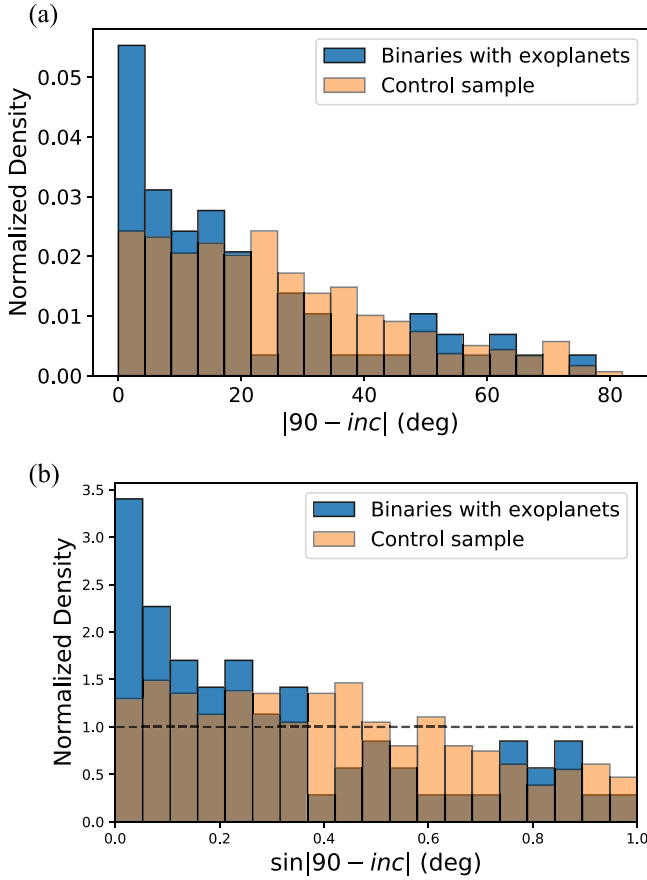
Figure 8. Histogram of $|90 - i|$ (a) and $\sin(|90 - i|)$ (b). We see an overabundance of systems with $i \approx 90°$ in our exoplanet sample compared to our control sample, indicating that there is some preferential alignment between the orbital planes of close-in exoplanets and visual binaries. We also find that the inclinations of binaries in our control sample are significantly different from the expected purely random $\sin(i)$ distribution (the dashed line in (b)), likely due to either selection effects (El-Badry & Rix 2018) or biases from inferring orbits from short arcs (Ferrer-Chávez et al. 2021).

evidence for a difference between the distributions, but with lesser significance: $p = 0.0172$.

The standard deviation in inclination is on average 14°, and a large proportion of samples have a skewed distribution of error. Additionally, error varies with inclination. The distribution of errors in our sample is shown in Figure 12(a), and the dependence of error on inclination in Figure 12(b). To explore the effect of this large and often asymmetrical error on the results of the K-S test, we perform a bootstrap procedure on the two distributions where we take a random sample from each binary system's LOFTI results and compare the overall distributions of those random samples. We repeat this process 10,000 times to derive a bootstrap distribution. This process calculates the distribution of p-values that we would expect to measure if we ran the same experiment many times, with slightly larger uncertainties on the inclinations (by about a factor of $\sqrt{2}$). We found that when we performed this analysis comparing the full samples, 61.91% of the bootstrap instances yielded a p-value less than 0.05, with the median p-value being 0.0300. We run the same bootstrap test on the subset of systems with $a < 700$ au. This test returns a median p-value of 0.0044, with 87.35% of the bootstrap instances being at least $p = 0.05$.

(a)

(b)
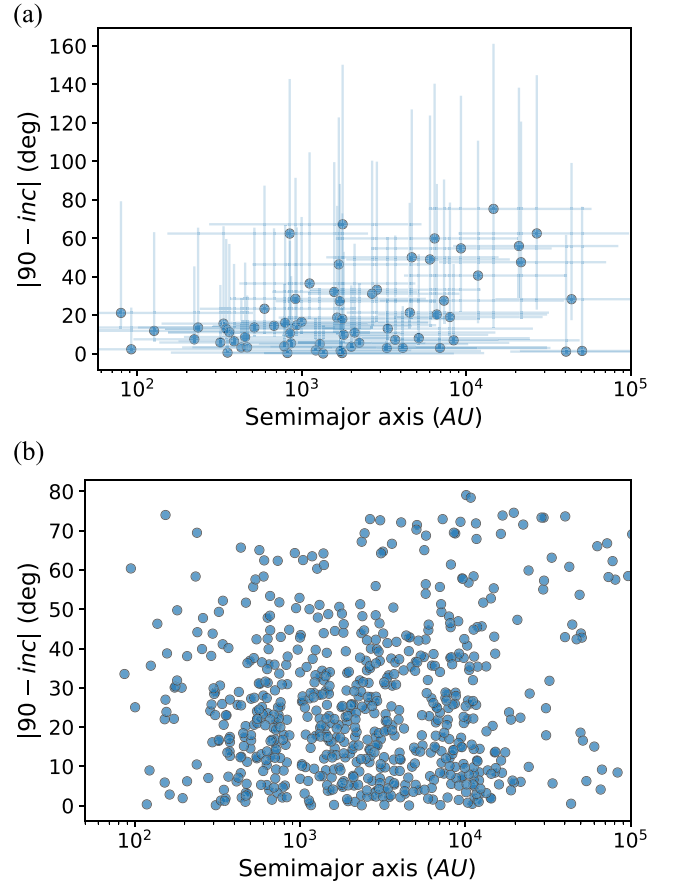
Figure 9. A clear alignment of binary and exoplanet below approximately 700 au is seen in (a), the sample with exoplanet candidates. No such alignment below 700 au is seen in (b), the control sample.
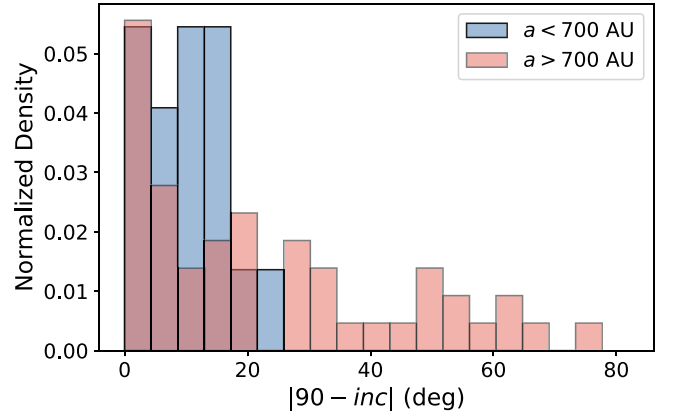
Figure 10. Distribution of $|90 - i|$ (with median i) for binaries with exoplanets with semimajor axes (a) below and above 700 au. The binaries with semimajor axes less than 700 au are clustered within 20° of edge-on orbits, while the binaries with semimajor axes greater than 700 show a more uniform distribution of inclinations.

We also simulated a K-S test of two $\sin(90 - i)$ probability density functions with sample sizes similar to those of that in our study and various types of skewed error (e.g., skewed away from $i = 90$ or toward $i = 90$). All simulations returned uniform distributions of K-S p-values, indicating that any skewed error is likely not affecting the result of the K-S test.

For completeness, we tested whether the distribution of binary inclinations in the control sample is consistent with
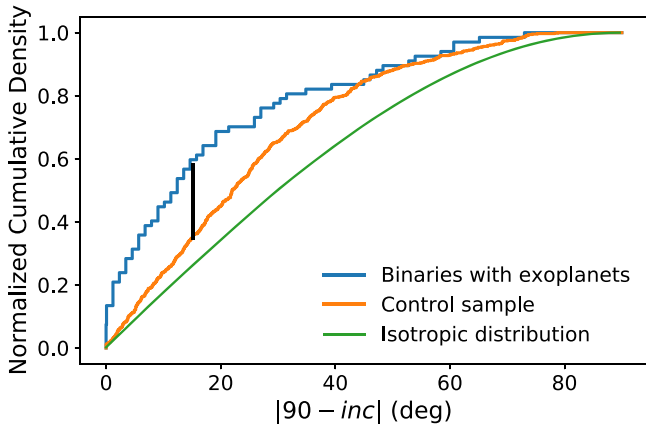
Figure 11. The two empirical cumulative distributions used in the Kolmogorov–Smirnov (K-S) test. The black line shows the maximum distance between the two distributions which corresponds to a K-S value of 0.223 and a *p*-value of 0.0037.

Figure 12. A histogram (a) and scatterplot (b) showing the error in inclination's distribution and dependence on $90 - i$, respectively. The noticeable difference in the errors of (a) is likely caused by more-aligned systems, which are more prevalent in the sample with exoplanets, tending to have tighter constraints on inclination.

randomly oriented orbits. The expected probability density function of binary inclination angles for random orbital orientations is proportional to $\sin(i)$. When we compare the control sample to inclinations drawn from a $\sin(i)$ distribution with a K-S test, we find a significant difference between the

Figure 13. The median inclination relative to 90° vs. median eccentricity for the control sample. A degeneracy exists between inclination and eccentricity, excluding any systems with inclination near 90° and low eccentricity.

two. We show a comparison of the control sample distribution and the expected isotropic distribution in Figures 8(b) and 11. This difference is likely caused by either subtle biases when fitting astrometric orbits in small-orbit arc fitting (Ferrer-Chávez et al. 2021) or selection effects in the El-Badry & Rix (2018) catalog. The control sample has slightly fewer face-on systems and more edge-on systems than we would expect from a perfectly random distribution of inclinations. Nevertheless, the difference between the distribution of inclinations in the control sample and the sample of binaries with exoplanets is still significant.

4.1.1. Inclination–Eccentricity Degeneracy

There is an apparent degeneracy between inclination and eccentricity, presumably related to the bias mentioned in Ferrer-Chávez et al. (2021). We plot inclination versus eccentricity for our systems in Figure 13, where it is clear that LOFTI does not find any systems with low eccentricity and inclination near 90°. This is not a feature of the OFTI method specifically: all orbits derived through short-arc fitting will have a similar degeneracy between median inclination and eccentricity. Such a degeneracy is only between summary statistics of eccentricity and inclination. The full parameter space is covered among all individual samples.

We have no reason to suspect that the eccentricity of the binary orbit could somehow be preferentially modifying the orbit of the planet, so do not believe that this degeneracy can explain the overabundance of systems with inclination near 90°. In fact, the difference in the distribution of eccentricity in the control sample versus the sample with exoplanets is not statistically significant ($p = 0.119$).

4.2. Mixture Model

We fit a mixture model to the orbital inclinations in our sample of binaries with planets in an attempt to determine what fraction of the binary systems with exoplanets can be explained by a random distribution versus what fraction is aligned. The probability density function of i can be expressed as $\sin(i)$ (although selection effects slightly bias the distribution, as shown in the previous section), while we represent the distribution of the aligned binaries' inclinations as a normal
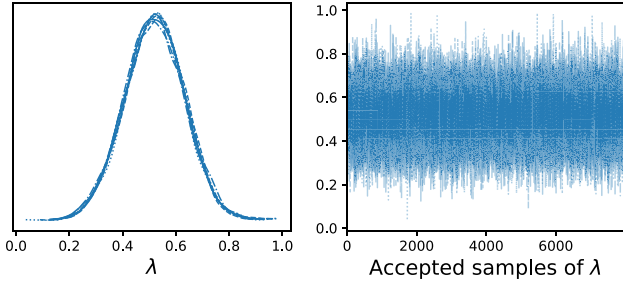
Figure 14. The posterior probability distribution of the mixture parameter λ for eight chains and the accepted samples of λ. Our mixture model fit prefers a roughly 50%/50% ratio of systems in an aligned Gaussian population to those in a random $\sin(i)$ distribution.

distribution. Our likelihood function is defined as

$$p(y|\lambda, \sigma) = \prod_{n=1}^{N} (\lambda \cdot \mathcal{N}(y_n|\mu, \sigma) + (1 - \lambda) \cdot \sin y_n), \quad (4)$$

where y are the binary orbital inclinations, $\mathcal{N}$ is a normal distribution with mean μ and standard deviation σ, and λ is the mixture parameter or the fraction of systems in the aligned population. We impose the following priors: μ is fixed to be $\pi/2$ radians (perfectly aligned with the planet orbits), σ is constrained with a half-normal distribution with standard deviation $\frac{\pi}{2}$ radians, and λ, the mixture parameter, has a uniform prior from 0 to 1. Specifically,

$$\sigma \sim \mathrm{Normal}(0, \frac{\pi}{2}), \quad (5)$$

$$\sigma > 0, \quad (6)$$

$$\lambda \sim \mathrm{Uniform}(0, 1), \quad (7)$$

$$\mu = \pi/2. \quad (8)$$

We run the mixture model in the probabilistic programming language Stan (Riddell et al. 2018). The resultant distribution of λ is peaked near 50%, with the 90% confidence interval being [0.33,0.72]. Though the 90% confidence interval is fairly wide, it does allow us to conclude that, assuming our Gaussian + $\sin(i)$ model for the distribution is a reasonable approximation, the process of alignment occurs in between 26% and 72% of the systems in our sample with 90% confidence.

4.3. Assessing Possible Biases

While we were careful to construct a control sample of binaries with nearly identical properties to the exoplaet sample, there are a few subtle differences that could plausibly introduce a difference in the distribution of inclinations. Here, we show that these differences do not significantly affect the distribution of inclination angles within the control sample, and therefore are highly unlikely to significantly contribute to the apparent alignment between planetary systems and wide-binary orbits.

4.3.1. Metallicity Measurements

Some of the binary systems with exoplanets have metallicity measurements from our own TFOP follow-up spectroscopic observations (see Section 2.3.1). We do not have metallicity measurements for any binaries in the control sample aside from those with archival observations identified
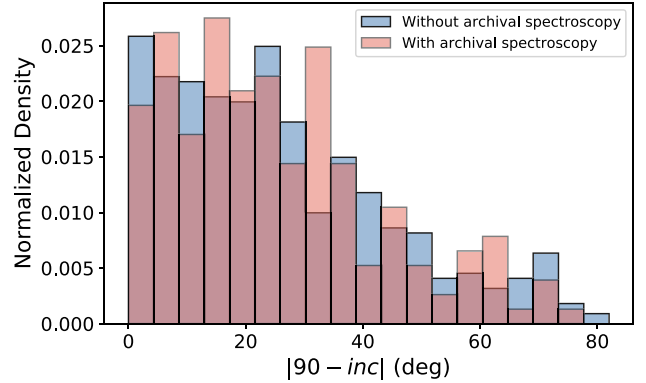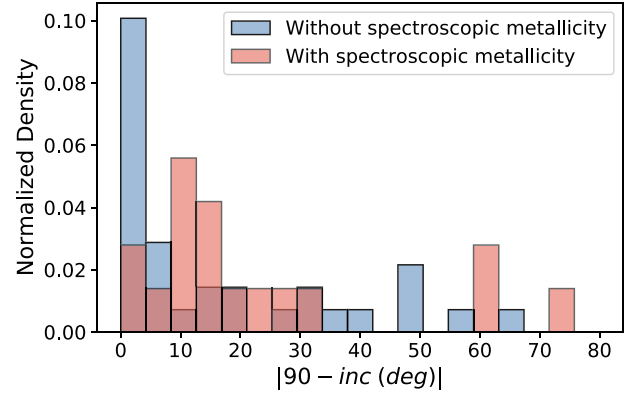
Figure 15. A comparison of binaries with exoplanets with and without spectroscopic metallicity measurements from TFOP (a) and the binaries in the control sample with and without archival spectroscopy (which metallicity is derived from). Neither comparison shows a statistically significant difference, so differences in metallicity measurements are unlikely to explain the difference in the inclination distributions between the exoplanet and control sample.

by El-Badry & Rix (2019), so it is plausible that including the TFOP spectroscopy could introduce a small difference between the samples. To test this, we compare the inclination distributions of binary systems with spectroscopic metallicity measurements to those without using a K-S test.

First, we tested whether there is a significant difference between the inclination distribution of binaries with and without TFOP spectroscopy in our exoplanet sample. A K-S test reveals no statistically significant difference between these two subsamples ($p = 0.32$). In fact, if anything, the addition of spectroscopy leads to less of an alignment, as can be seen in Figure 15(a).

We also tested whether there is a significant difference between the inclination distribution of binaries with and without archival spectroscopic metallicity measurements in our control sample. Here, the K-S test also reveals no statistically significant difference between those samples in the control sample with and without archival spectroscopy (Section 2.3.1) as can be seen in Figure 15(b) ($p = 0.699$).

These tests show that, evidently, the presence or absence of a spectroscopic metallicity measurement has a negligible impact on the resulting distribution of binary orbital inclinations. This effect is therefore highly unlikely to explain the apparent alignment of wide-binary orbits with their planetary systems.
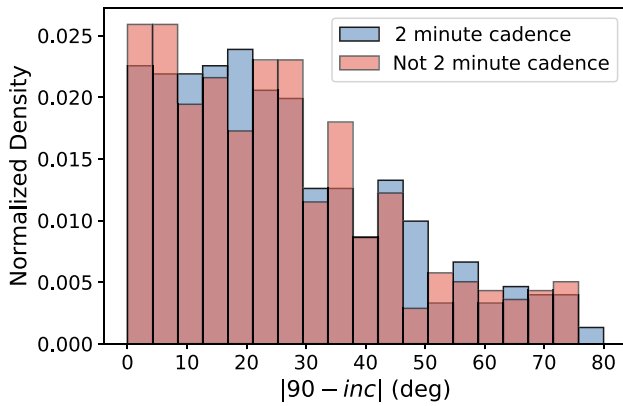
Figure 16. A comparison in the distribution of inclinations in binary systems in the control sample with 2 minute cadence and those without. The two distributions are essentially indistinguishable, so selection biases from the TESS 2 minute target selection are unlikely to affect our results.

4.3.2. 2 Minute Cadence versus FFI Light Curves

As described in Section 2.1.1, TESS observes 20,000 of the best planet-search target stars at 2 minutes cadence (Barclay et al. 2018; Stassun et al. 2019) per sector, while the rest of the sky is observed at 30 minutes cadence (and more recently, at 10 minutes cadence in the extended mission). One of the selection criteria for 2 minute cadence observations is the extent to which nearby stars dilute the signal of the target star. Therefore, stars chosen for 2 minute cadence observations were less likely to be nearby other bright stars, potentially including visual binary companions. This could lead to an increase in edge-on binaries in 2 minute cadence observation since companions could be more likely to be very close to the primary star, and therefore less likely to be resolved in ground-based, seeing-limited imaging and consequently less likely to be rejected due to the companion's flux dilution. Because transit searches in 2 minute cadence observations are more sensitive to detecting planet candidates, this could plausibly introduce a bias in our results.

We tested whether the selection of 2 minute targets significantly affects the inclination distribution of wide-binary companions by comparing the distributions of stars in our control sample that were and were not observed in 2 minute cadence mode. As demonstrated in Figure 16, we find no significant difference in the distribution of inclinations for stars in the control sample observed in 2 minute cadence. A K-S test fails to reject the null hypothesis that binary inclinations for stars observed at 2 minute cadence and those observed in FFIs are drawn from the same population ($p = 0.85$). The TESS 2 minute cadence target selection is therefore highly unlikely to be a source of bias.

4.3.3. Additional Biases

Visual binary stars that are not resolved by TESS introduce complex biases into transiting exoplanet detection that might plausibly affect the measured binary inclination distribution (Bouma et al. 2018). In our study, 45 systems have separations less than 30″, the approximate resolution of TESS. In this case, however, the difference in detectability of exoplanets in visual binary systems that are resolved in TESS versus those that are not resolved should not cause a preferential alignment between exoplanet and binary system. A larger fraction of binary systems that have face-on orbits with respect to the plane of the sky are expected to be resolved by TESS than those with

edge-on orbits. Thus, if anything, the larger fraction of resolved misaligned systems would cause the opposite effect from what we observe.

It is known that because LOFTI is inferring orbits from such short orbital arcs, inferred orbits can preferentially be biased toward higher inclinations (i.e., toward $i = 90$, an alignment with the location of the planetary systems in our study; Ferrer-Chávez et al. 2021). However, there is no reason to suspect that this bias is affecting the sample with exoplanets anymore than the control sample.

5. Dynamical Mechanisms to Explain the Existence of the Preferential Alignment

In this section, we discuss two possible dynamical mechanisms that could explain a preferential alignment between visual binaries and the planets in those systems.

5.1. Lidov–Kozai Timescale

The Lidov–Kozai mechanism induces oscillations in a pair of objects (in this case the planet and star) from the secular influence of a massive, faraway companion. Bodies undergoing the Lidov–Kozai effect experience oscillations in their inclination and eccentricity, trading off between the two quantities on a characteristic timescale set by the system parameters. The Lidov–Kozai mechanism has been invoked to explain a wide variety of astrophysical phenomena, including the existence of hot Jupiters (Fabrycky & Tremaine 2007; Naoz et al. 2012; Dawson & Johnson 2018; Li et al. 2020).

Since the planet mass is much smaller than the inner stellar mass, the Lidov–Kozai effect will only drive substantial dynamical evolution when there is a significant mutual inclination ($\gtrsim 40°$) between the orbit of the planet–star system and the orbit of the distant binary companion (Naoz et al. 2013). The fact that the Lidov–Kozai effect operates on systems with large mutual inclinations means that it could plausibly explain the alignment we observe between the orbits of wide-binary stars and their close-in planetary systems. If, for example, the inclinations of wide-binary orbits were randomly distributed with respect to the orbits of the planetary system, the Lidov–Kozai effect would only act to significantly alter the geometries of systems with large initial misalignments. If the Lidov–Kozai effect preferentially disrupts systems with large initial misalignments (either by driving the eccentricity high enough to cause a collision between the planet and the star, or by causing dynamical instabilities that lead to planetary collisions or ejections), the resultant observed distribution of relative inclinations could develop some nonuniformity, as seen in our sample.

To assess whether the Lidov–Kozai effect could explain the alignment between wide-binary orbits and planetary orbits we observe, we calculate the timescale for Lidov–Kozai oscillations to take place for each system, assuming a large enough primordial mutual inclination for the effect to take place. If the Lidov–Kozai timescale is significantly smaller than the total system age, it could have acted to sculpt the observed alignment. The oscillations induced by the Lidov–Kozai timescale occur on a characteristic timescale, $\tau_{\rm LK}$, which can be estimated as

$$\tau_{\rm LK} \approx \frac{8}{15\pi} \left(1 + \frac{m_h}{m_c}\right) \left(\frac{P_c^2}{P_p}\right) (1 - e_p^2)^{(3/2)}, \qquad (9)$$
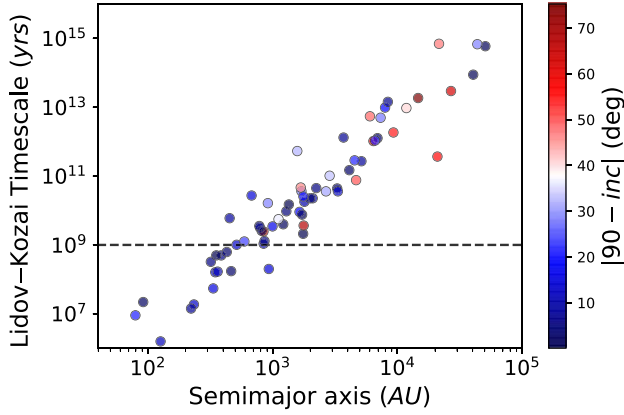
Figure 17. Lidov–Kozai timescale for binary systems with exoplanets plotted against the semimajor axis of the binary companion. The color bar represents $|90° - i|$ for each system. The dashed line represents the approximate ages of the stars (∼1 Gyr). The wide binaries with semimajor axes less than about 700 au are close enough that the Kozai–Lidov effect could operate on similar timescales, but other factors make this explanation for the alignment less likely.

where m_h is the mass of the planet host star (i.e., the primary star), m_c is the mass of the stellar companion, P_c is the period of the binary companion, P_p is the period of the planet, and e_p is the eccentricity of the planet (Holman et al. 1997; Antognini 2015). The period of the planet is very small compared to the mutual period of the stars. We calculate the Lidov–Kozai timescale for each system in our sample and show the results in Figure 17 as a function of the semimajor axis of the binary system.

We find that in systems where the Lidov–Kozai timescale is significantly less than the total age of the system (the systems below the dashed line in Figure 17) the systems are preferentially aligned. This is a consequence of the fact that most systems with binary semimajor axes smaller than about 700 au tend to have orbits aligned with their planetary systems in our sample. As a result, it is plausible that the Lidov–Kozai effect would operate rapidly enough in systems below 700 au to contribute to the alignment we see.

However, we suspect that the Lidov–Kozai effect is likely not a dominant effect causing the observed alignment between binary and planetary orbital planes. One reason is that for planets orbiting very close to their stars, even small apsidal precession rates (due to either general relativity, tides, or the stellar quadrupole moment) can completely suppress the Lidov–Kozai effect (Sterne 1939; Murray & Dermott 1999; Fabrycky & Tremaine 2007). Also, any sculpting by the Lidov–Kozai effect would tend to leave systems with mutual inclinations with up to 40° misalignments, while the overdensity of aligned systems in our sample is strongest within 10° of alignment. Thus, it is likely that if the Lidov–Kozai effect is acting in systems, the effect is quite small and would need to be coupled with other effects to explain the observed alignment.

5.2. Disk Timescale

Another process that could explain the preferential alignment of wide-binary orbits with their close-in planetary systems is that the gravitational influence of the wide-binary star could torque the protoplanetary disk into alignment early in the system's history. Consider, for example, a wide-binary companion in an initially misaligned orbit around a star with a

gas-rich protoplanetary disk. The mechanism of Batygin (2012; see also Bate et al. 2000) could be induced by the wide-binary companion, causing the protoplanetary disk to precess in the reference frame of the binary-star system, which would manifest as an oscillation of inclination in the reference frame of the host star's angular momentum vector. As the protoplanetary disk precesses, it can simultaneously dissipate energy and move toward its lowest-energy state, an alignment with the binary-star angular momentum and disk angular momentum vectors (Bate et al. 2000; Martin & Lubow 2017). Any planets that subsequently form from the disk would tend to be in well-aligned orbits with the wide-binary companion.

The warping of a disk can lead to dissipation of energy in the disk. The effect of this warping on the alignment of the disk has been studied in Bate et al. (2000) and Zanazzi & Lai (2018) in a gaseous disk. The timescale of alignment due to warping of the gaseous disk may be compatible with the timescales we observe assuming an outer disk radius of approximately 100 au according to Zanazzi & Lai (2018). However, it is well known that any gas disk, regardless of warping, will thermalize energy due to turbulence or viscosity (Nelson et al. 2000; D'Alessio et al. 2006). As a disk radiates away this energy during precession, it will move to its lowest-energy state, an alignment with the binary-star system.

To explore the possibility that the disk is dissipating energy and moving toward an alignment via a precession, we use the approximate closed-form expression of Batygin's (2012) supplementary materials Equation (6) to estimate the timescale of one precession, and thus one cycle of oscillation in inclination. The timescale of precession is not the same as the timescale of alignment, but given that sufficiently fast precession is a necessary condition for alignment, this timescale can be used to somewhat estimate if alignment could take place in the systems in our sample. Batygin (2012) gives

$$\frac{d\Omega_{disk}}{dt} = -\frac{\int_{a_{in}}^{a_{out}} G\Sigma(r) M_c \left(\frac{r}{a_c}\right)^2 \tilde{b}_{3/2}^{(1)}(0.95)\, dr}{4\int_{a_{in}}^{a_{out}} \Sigma(r)\sqrt{GM_\star r^3}\, dr}\cos(i), \quad (10)$$

where a_c and M_c are the semimajor axis and mass of the companion star, respectively, $M_\star$ is the mass of the host star, i is the inclination of the disk with respect to the binary orbit, $\Sigma(r)$ is the disk density profile, a_{out} and a_{in} are the inner and outer boundaries of the disk, and $\tilde{b}_{3/2}^{(1)}$ is a Laplace coefficient with disk softening (see Batygin 2012, supplementary materials Equation (4) for details). Since binaries with smaller separations tend to have smaller outer disk radii (Manara et al. 2019), we calculate all disk timescales for a_{out} in the range $[a_b^*0.05, a_b^*0.25]$ if $a_b < 400$ and otherwise [20, 100], where a_b is the semimajor axis of the binary-star system. Manara et al. (2019) calculated the dust radii of disks, but the gas radii of disks (which is most responsive to torques) is expected to be larger than the dust radius, although the two tend to be proportional (Ansdell et al. 2018). In general, τ_Ω has a very weak dependence upon the value of a_{out} as long as a_{out} is within a reasonable range of values. We use a density profile of the form

$$\Sigma(r) = \Sigma_c \left(\frac{r}{R_c}\right)^\gamma \exp\left[-\left(\frac{r}{R_c}\right)^{2-\gamma}\right], \quad (11)$$
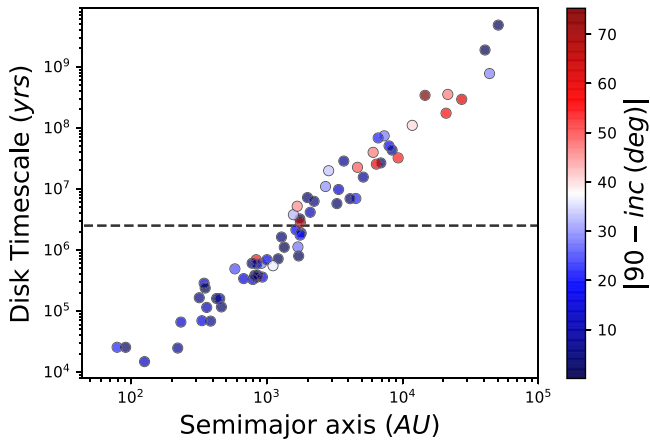
Figure 18. The disk precession timescale as simulated for the sample of binary-star systems with exoplanets. The horizontal dashed line indicates the typical 2.5 Myr half-lifetime of protoplanetary disks (Mamajek 2009). The well-aligned sample of binaries with semimajor axes shorter than about 700 au typically have disk precession timescales short enough that this mechanism could explain the alignment.

where γ is 0.9 (Andrews et al. 2010) and R_c is 110 au, the mean Andrews et al. (2010) value. Assuming the parameters of Equation (10) do not vary greatly over the precession cycle, the timescale of one complete precession cycle can be estimated as

$$\tau_\Omega = \pi^2 \left(\frac{4 \int_{a_{\text{in}}}^{a_{\text{out}}} \Sigma(r) \sqrt{GM_\star r^3}\, dr}{\int_{a_{\text{in}}}^{a_{\text{out}}} G\Sigma(r) M_c \left(\frac{r}{a_c}\right)^2 \tilde{b}_{3/2}^{(1)}(0.95)\, dr} \right). \qquad (12)$$

Here, Equation (12) is averaged over possible inclination values (the mean of $\cos^{-1}(i)$ for isotropic inclinations is $\pi/2$). We calculated the disk precession timescales for each system in our sample and show the resulting timescales in Figure 18. We find that systems with disk precession timescales less than a few megayears tend to be preferentially aligned, while systems with longer precession timescales show more large misalignments. It is noteworthy that a timescale of a few megayears happens to be the typical lifetime for protoplanetary disks (Mamajek 2009), indicating that this mechanism could explain both the existence of an alignment and the greater level of alignment for binaries closer than about 700 au.

6. Discussion

Using data from the TESS and Gaia space missions, along with ground-based follow-up observations, we have shown that the orbits of wide-binary stars with transiting exoplanets are significantly more likely to have an inclination near 90° than randomly selected binary systems. Inclination is equal to the minimum possible alignment between binary orbit and exoplanet orbit, so an excess of inclinations near 90° for transiting planet-hosting systems, as compared to those without known transiting planets, suggests an underlying physical process that results in preferential alignment between outer stellar companions and inner transiting planets. Understanding the origin of such a preferential alignment will have implications for understanding the formation and evolution of both planets and binary stars. Here, we discuss three possible ways in which such an alignment may have come to be.

6.1. Possibility 1: Primordial Alignment

One possibility is that the alignment between wide-binary and close-in planetary orbits is primordial. That is, the planets and binary each formed in nearly their current aligned configuration. Binary-star systems at relatively low separations can form through disk fragmentation and turbulent fragmentation. In disk fragmentation, the initial gravitationally unstable circumstellar disk fragments during the collapse of the system, forming a binary or higher-multiplicity system (Adams et al. 1989; Bonnell & Bate 1994; Sigalotti et al. 2018). Disk fragmentation is expected to form binary systems where the stellar angular momenta are aligned with the binary orbit and the plane of the protoplanetary disk. Evidence for disk fragmentation includes aligned bipolar outflows (Tobin et al. 2013) and the metallicity-dependent binary fraction (El-Badry & Rix 2018). Recent observations have shown that disk fragmentation primarily takes place for binary stars with semimajor axes less than about 200 au (Tobin et al. 2016; El-Badry & Rix 2019). More distant binaries likely formed via only turbulent fragmentation, which is not necessarily expected to produce binary stars with orbits in the same plane as any planetary system. Such systems can also migrate to smaller separations (i.e., below 200 au).

One way to explain our observation that there appears to be a preferential alignment between wide binaries and planets, and that the alignment is most prominent for binary stars with semimajor axes less than 700 au, is that close-in binaries form aligned with the protoplanetary disk, while more distant binaries form via a different mechanism that leaves their orbits misaligned. In this case, presumably this would imply that the close-in binaries in our sample formed mainly via disk fragmentation, while the more distant binaries formed via turbulent fragmentation and, more rarely, capture of the binary companion. If this were true, it would would necessitate that most binaries with semimajor axes less than 700 au formed from disk fragmentation, which would be in tension with the apparent ~200 au cutoff for disk fragmentation (Tobin et al. 2016; El-Badry & Rix 2018), as well as the fact that some binaries below 200 au should have formed via turbulent fragmentation and later migrated inwards.

6.2. Possibility 2: Dynamically Sculpted Binary Orbit Misalignment

If the binaries in our system tend to all form aligned (which is not supported by the observed occurrence of turbulent fragmentation at separations similar to those seen in our study), then the binary orbits of the systems above the threshold ~700 au could be sculpted by the dynamical influence of passing stars. Deacon & Kraus (2020) have shown that wide binaries are rare in open clusters, suggesting that open clusters are a highly dynamical environment. Before complete disruption of a binary system, the system can be dynamically perturbed, leading to the larger fraction of misaligned systems we see above ~700 au. Such a dynamical sculpting need not take place in only clusters: Kaib et al. (2013) found that the orbits of binary systems can be altered by the galactic tide and passing stars even when systems are not in clusters.

However, as discussed in Section 6.1, observational evidence suggests that aligned systems form primarily below 200 au and thus the cutoff is probably not primarily due to a dynamical sculpting of the binary orbits.

6.3. Possibility 3: Dynamically Sculpted Alignment

The final possibility we consider is that some dynamical process has sculpted the population of planets in wide binaries into orbital alignment after formation. Wide-binary systems with separations similar to those probed in this work are expected to form primarily via turbulent fragmentation, where turbulence fractures the initial stellar core into multiple separate overdensities (Offner et al. 2010, 2016; Bate 2018). In turbulent fragmentation, the two stars tend to have a distribution of angular momentum vectors that is less aligned on average than disk fragmentation (Offner et al. 2016; Bate 2018). However, a larger portion of binaries that form via turbulent fragmentation are still expected to have aligned orbits than a completely isotropic distribution (Bate 2018). Indirect evidence for turbulent fragmentation in wide-binary systems includes outflow orientations (Lee et al. 2016) and direct imaging (Fernández-López et al. 2017).

The initial misalignment of some binary systems that form via turbulent fragmentation will cause the disk to precess by the mechanism described in Section 5.2, dissipate energy, and lead to an alignment between the disk and binary orbit. This scenario seems like it could explain both the observed alignment and the transition from predominantly aligned systems to more misaligned systems around ∼700 au, which corresponds to a disk precession timescale similar to the lifetime of protoplanetary disks.

6.4. Future Work

We have presented evidence showing that the orbits of wide-binary stars are preferentially aligned with the orbits of close-in planets in those systems. Although the alignment appears to be statistically significant, it is based on a relatively small sample of planetary systems. Confirming the conclusions of this work with a larger sample of binary stars hosting transiting exoplanets would be highly valuable.

Fortunately, it should be straightforward to increase the size of our sample. Recently, El-Badry et al. (2021) released a sample of over a million wide-binary stars from Gaia EDR3, including 274 visual binaries found to have exoplanets by TESS as of 2021 February 1. With this new sample of binaries, it will be possible to triple the size of our current sample. In addition, with improved Gaia astrometry from future data releases, such as more systems with radial velocity and an astrometric acceleration term, the inclinations of systems can be better constrained. If our hypothesis that most of the binaries form via turbulent fragmentation and were dynamically sculpted into aligned systems is true, then the statistical significance of the difference in inclination distribution of binaries above and below 700 au should increase, and a clearer dividing timescale between aligned and randomly distributed systems should emerge.

A larger sample of binaries will also make it possible to subdivide the sample and look for correlations with planetary parameters. For example, initially misaligned wide-binary companions could help trigger the formation of hot Jupiters via Lidov–Kozai oscillations, so it would be interesting to see whether the inclinations of wide-binary companions in hot Jupiter systems are different from those in systems with small planets. Another important characteristic to investigate is the transiting planet system multiplicity. Compact multiplanet-systems' planets are susceptible to inclination oscillations from exterior companions that can change the planet's mutual inclinations enough to prevent them all from transiting (Becker & Adams 2017).

Another valuable avenue may be to make similar measurements for different samples of planetary systems. For example, ground-based, high-resolution imaging observations of binaries too close to be resolved by Gaia can help determine whether binaries with semimajor axes less than those probed in this work ($a \lesssim 100$ au) also show preferential alignment. It may also be possible to increase the sample of particularly wide binaries ($a \gtrsim 1000$ au) by including planet candidates orbiting the more distant stars targeted by Kepler and K2 that reside in binary systems, which can be resolved by Gaia.

Finally, we note that as follow-up of TESS planets continues, the purity of the TESS planet-candidate sample will increase and systematics in TESS planet detection will become better understood. The ongoing TFOP observation campaign will continue identifying false positives among the TESS planet-candidate sample and increase the likelihood that any given candidate in the surviving sample is indeed a planet candidate. Identifying these false positives will remove noise from the distribution of wide-binary inclinations. As the systematics in TESS planet detection become better understood, it can be determined with a higher degree of confidence whether the observed alignment is affected by a bias in TESS's detection method.

7. Conclusion

Given the high frequency of wide-binary systems, understanding the evolution of protoplanetary disks and, later, planets, is important to having an holistic understanding of planet formation and evolution. Various dynamical effects have been proposed for wide-binary systems (e.g., Wu & Murray 2003; Batygin 2012), but observational studies of planets in wide-binary systems are sparse, limiting the confirmation of these dynamical effects.

We conducted a study of planets in wide-binary systems and demonstrated that the orbits of wide binaries and planets residing in the binaries are aligned ($p = 0.0037$). We first gathered a sample of wide-binary systems with exoplanets along with a control sample with matching properties (Section 2). We then derived stellar masses (Section 3.1) and estimated probable orbits for the wide-binary systems (Section 3.2). We found that there was a statistically significant overabundance of systems around $i = 90$, suggesting that planets and the wide-binary systems they reside in tend to be aligned (Section 4.1). We found that the alignment appears to occur primarily in systems with binary semimajor axes less than ∼700 au.

We then presented a mixture model to attempt to derive the amount of wide binaries that are aligned (Section 4.2). Although the results were relatively uninformative, it is likely that about half of the systems in our sample are aligned (with at least 25% alignment at 97.5% confidence). We found that no biases we could identify were causing the alignment (Section 4.3).

We derived Lidov–Kozai timescales for the binary systems with planets (Section 5.1). Additionally, we estimated the disk precession timescale (Batygin 2012) for the systems (Section 5.2). We observed that in the case of the disk precession mechanism, almost all misaligned systems have disk precession timescales greater than the typical age of protoplanetary disks.

Finally, we discussed possible mechanisms for the observed alignment (Section 6). The binary systems that form via disk fragmentation are expected to be aligned initially, while the binary systems that form via turbulent fragmentation and capture should have a more or less isotropic distribution of alignments. In order to explain an alignment for the binary systems that form via turbulent fragmentation, we proposed that the disk mechanism and, to a lesser extent, the Lidov–Kozai effect can lead to preferential alignment of these systems early in their lifetime (Section 6.3).

As more exoplanets are discovered by TESS, the effects observed in this study are worth revisiting. Particularly, with a larger sample, in the future we could conclusively detect the alignment, probe the effect of parameters like planet mass or multiplicity, and more conclusively determine whether the alignment is stronger for binary systems with semimajor axes less than $\sim$700 au.

Facilities: Gaia, TESS, FLWO:1.5 m (TRES), CTIO:1.5 m (CHIRON), UKST (RAVE), LCOGT (NRES), FIES, LAMOST, APOGEE, GALAH, ASTEP (Guillot et al. 2015), MuSCAT (Narita et al. 2015), MuSCAT2 (Narita et al. 2019), MuSCAT3 (Narita et al. 2020), SIRIUS (Nagayama et al. 2003).

Software: LOFTI (Pearce et al. 2020), Astropy (Price-Whelan et al. 2018), Pystan (Riddell et al. 2018), Isochrones (Morton 2015), TOPCAT (Taylor 2006), AstroImageJ (Collins et al. 2017), TAPIR (Jensen 2013).

Appendix A
Full Corner Plot of Derived LOFTI Parameters

Figure A1 is a corner plot of a sample full-orbital fit from
LOFTI.

Figure A1. A corner plot of a sample full-orbital fit. Note that period and epoch of periastron passage (t_0) are calculated according to Table 2.

Appendix B
List of Binary Systems with Transiting Exoplanet Candidates

Table B1 contains the first three entries of the supplementary table of binaries with exoplanets. "1" designates the host star, while "2" designates the companion star.

1. *EDR3designation1*—GAIA EDR3 designation 1
2. *EDR3designation2*—GAIA EDR3 designation 2
3. *ra1*—Right ascension 1 from Gaia
4. *ra2*—Right ascension 2 from Gaia
5. *dec1*—decl. 1 from Gaia
6. *dec2*—decl. 2 from Gaia
7. *pmra1*—Proper motion in direction of R.A. 1 from Gaia
8. *pmra2*—Proper motion in direction of R.A. 2 from Gaia
9. *pmdec1*—Proper motion in direction of decl. 1 from Gaia
10. *pmdec2*—Proper motion in direction of decl. 2 from Gaia
11. *rv1*—Radial velocity 1 from Gaia
12. *rv2*—Radial velocity 2 from Gaia
13. *feh1*—Metallicity 1 from various sources
14. *feh2*—Metallicity 2 from various sources
15. *logg1*—log(g) 1 from various sources
16. *logg2*—log(g) 2 from various sources
17. *Teff1*—Effective Temperature 1 from various sources
18. *Teff2*—Effective Temperature 2 from various sources
19. *Gmag1*—Gaia *G*-band magnitude 1
20. *Gmag2*—Gaia *G*-band magnitude 2
21. *BPmag1*—Gaia *BP*-band magnitude 1
22. *BPmag2*—Gaia *BP*-band magnitude 2
23. *RPmag1*—Gaia *RP*-band magnitude 1
24. *RPmag2*—Gaia RP-band magnitude 2
25. *Kmag1*—*K* magnitude 1 from 2MASS
26. *Jmag1*—*J* magnitude 1 from 2MASS
27. *Hmag1*—*H* magnitude 1 from 2MASS
28. *Kmag2*—*K* magnitude 2 from 2MASS
29. *Jmag2*—*J* magnitude 2 from 2MASS
30. *Hmag2*—*H* magnitude 2 from 2MASS
31. *parallax*—parallax (of primary star but taken to be of entire system) from Gaia
32. *TIC1*—TESS Input Catalog Identifier 1
33. *TIC2*—TESS Input Catalog Identifier 2
34. *inclination*—Inclination of binary system from LOFTI
35. *ecc*—eccentricity of binary system from LOFTI
36. *semimajor axis*—semimajor axis of binary system from LOFTI
37. *long. asc. node*—longitude of ascending node of binary system from LOFTI
38. *arg. per.*—argument of periastron of binary system from LOFTI
39. *period (binary)*—orbital period of binary system from LOFTI
40. *epoch per.*—Epoch of periastron passage from LOFTI
41. *mass 1*—mass of star 1 from `isochrones`
42. *mass 2*—mass of star 2 from `isochrones`
43. *radius (planet)*—radius of planet from TESS
44. *period (planet)*—orbital period of planet, from TESS

Table B1
Binaries with Exoplanets

	(1) EDR3designation1	(2) EDR3designation2	(3) R.A.1 (deg)	(4) R.A.2 (deg)	(5) Decl.1 (deg)	(6) Decl.2 (deg)	(7) pmra1 (mas/year)	(8) pmra2 (mas/year)
0	4844691297067063424	4844691297067064576	62.9664	62.9549	-37.9397	-37.945	-11.061 ± 0.01	-11.481 ± 0.016
1	4903786336207800576	4903786336207800704	12.976	12.9711	-59.3436	-59.345	89.035 ± 0.013	89.778 ± 0.013
2	2983316311375470976	2983316311375257472	79.1022	79.1019	-15.5102	-15.5127	5.621 ± 0.017	4.457 ± 0.014

	(9) pmdec1 (mas/year)	(10) pmdec2 (mas/year)	(11) rv1 (km/s)	(12) rv2 (km/s)	(13) feh1 [Fe/H]	(14) feh2 [Fe/H]	(15) logg1 (cgs units)	(16) logg2 (cgs units)
0	12.347 ± 0.014	12.229 ± 0.023	18.539 ± 0.807		0.056 ± 0.1		4.645 ± 0.12	
1	-149.15 ± 0.014	-149.33 ± 0.014	10.35 ± 0.205	11.663 ± 0.334	0.48 ± 0.29	0.029 ± 0.08	4.81 ± 0.4	4.051 ± 0.12
2	-25.478 ± 0.016	-27.409 ± 0.014	-14.23 ± 0.352	-12.694 ± 0.339	0.09 ± 0.08		4.471 ± 0.08	

	(17) Teff1 (K)	(18) Teff2 (K)	(19) Gmag1	(20) Gmag2	(21) BPmag1	(22) BPmag2	(23) RPmag1	(24) RPmag2	(25) Kmag1	(26) Jmag1	(27) Hmag1
0	5439.1 ± 76.0		10.75	14.357	11.147	15.729	10.22	13.202	9.19	9.636	9.287
1	5815.2 ± 275.0	4908.2 ± 64.0	9.684	10.845	10.068	11.351	9.175	10.217	8.171	8.601	8.25
2	5685.9 ± 57.0		10.041	10.815	10.401	11.259	9.554	10.243	8.584	8.995	8.769

	(28) Kmag2	(29) Jmag2	(30) Hmag2	(31) parallax (mas)	(32) TIC1	(33) TIC2	(34) inclination (deg)	(35) ecc	(36) semimajor axis (au)
0	10.76	11.642	10.992	8.115 ± 0.038	257605131	257605132	$81.959^{4.812}_{35.612}$	$0.528^{0.451}_{0.468}$	5141.6^{14043}_{2341}
1	8.887	9.487	9.028	10.484 ± 0.024	281781375	281781376	$104.8^{36.020}_{9.212}$	$0.727^{0.230}_{0.612}$	930.61^{4697}_{395}
2	9.056	9.543	9.169	8.775 ± 0.033	189013224	189013222	$62.718^{11.502}_{33.684}$	$0.784^{0.167}_{0.255}$	1698.1^{3125}_{691}

	(37) long. asc. node (deg)	(38) arg. per. (deg)	(39) period (binary) (yr)	(40) epoch per. (yr)	(41) mass 1 ($M_\odot$)	(42) mass 2 ($M_\odot$)	(43) radius (planet) $R_\oplus$	(44) period (planet) (days)
0	-120.15^{169}_{177}	180.01^{163}_{163}	$304200.0^{1888400}_{181910}$	$-79910.0^{48267}_{913630}$	0.916 ± 0.019	0.556 ± 0.013	3.734 ± 0.218	3.734 ± 0.218
1	-117.7^{173}_{178}	178.94^{155}_{154}	20910.0^{290060}_{11770}	-7267.6^{4195}_{131542}	1.016 ± 0.058	0.831 ± 0.023	2.248 ± 0.189	2.248 ± 0.189
2	18.55^{336}_{15}	69.616^{90}_{44}	49897.0^{189573}_{27106}	-870.98^{426}_{1701}	1.018 ± 0.039	0.889 ± 0.028	2.215 ± 0.176	2.215 ± 0.176

(This table is available in its entirety in machine-readable form.)

Appendix C
List of Binary Systems in Control Sample
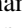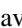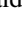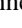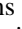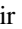
Table C1 contains the first three entries of the supplementary table of binaries in the control sample and has the same labels as Table B1. We define the primary star, labeled as "1" in the table, to be the star with the lower G-band magnitude.

Table C1
Control Sample

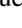| (1) EDR3designation1	(2) EDR3designation2	(3) R.A.1 (deg)	(4) R.A.2 (deg)	(5) Decl.1 (deg)	(6) Decl.2 (deg)	(7) pmra1 (mas/year)	(8) pmra2 (mas/year)
2773739877472213888	2773739877472214528	359.761	359.766	17.6387	17.6312	31.648 ± 0.0203	31.381 ± 0.0233
3693801002753319808	3693801002753320064	186.222	186.233	−2.8554	−2.85439	−58.988 ± 0.0256	−59.065 ± 0.0487
1206457348536232192	1206457172440176768	242.164	242.153	22.6489	22.6486	−14.923 ± 0.015273	−15.629 ± 0.0392

(9) pmdec1 (mas/year)	(10) pmdec2 (mas/year)	(11) rv1 (km/s)	(12) rv2 (km/s)	(13) feh1 [Fe/H]	(14) feh2 [Fe/H]	(15) logg1 (cgs units)	(16) logg2 (cgs units)
6.2133 ± 0.0088612	6.7162 ± 0.011475	22.079 ± 0.36532		0.114 ± 0.016		4.57 ± 0.03	
−11.219 ± 0.019061	−11.185 ± 0.034932	3.5139 ± 0.51263		0.158 ± 0.024		4.739 ± 0.044	
−58.423 ± 0.017962	−57.772 ± 0.046505	6.0017 ± 0.262		−0.49 ± 0.1		4.27 ± 0.1	

(17) Teff1 (K)	(18) Teff2 (K)	(19) Gmag1	(20) Gmag2	(21) BPmag1	(22) BPmag2	(23) RPmag1	(24) RPmag2	(25) Kmag1	(26) Jmag1	(27) Hmag1
5524.3 ± 19.08		10.724	14.269	11.123	15.357	10.192	13.237	9.148	9.571	9.222
5291.8 ± 28.98		11.209	15.748	11.675	17.361	10.627	14.502	9.428	9.913	9.493
5831.0 ± 100.0		9.8528	15.987	10.171	17.341	9.3953	14.825	8.52	8.84	8.587

(28) Kmag2	(29) Jmag2	(30) Hmag2	(31) parallax (mas)	(32) TIC1	(33) TIC2	(34) inclination (deg)	(35) ecc	(36) semimajor axis (au)
11.067	11.899	11.264	8.015 ± 0.043	238277444	238279987	$94.506^{28.104}_{3.167}$	$0.43977^{0.5473}_{0.4175}$	6254.1^{6696}_{3613}
11.921	12.741	12.159	8.1915 ± 0.091	94893802	94893801	$94.936^{27.804}_{12.0}$	$0.83977^{0.1534}_{0.7033}$	11363.0^{20422}_{8642}
12.397	13.258	12.657	7.9154 ± 0.065	103866841	103866840	$32.264^{23.685}_{23.1239}$	$0.72585^{0.1335}_{0.1495}$	9626.8^{10192}_{4596}

(37) long. asc. node (deg)	(38) arg. per. (deg)	(39) period (binary) (yrs)	(40) epoch per. (yrs)	(41) mass 1 ($M_\odot$)	(42) mass 2 ($M_\odot$)
$145.02^{168.84}_{178.654}$	$179.64^{166.24}_{168.798}$	307960^{905340}_{196220}	$-159040^{114937}_{670350}$	0.95091 ± 0.0138	0.511 ± 0.0121
$84.996^{179.254}_{179.351}$	$179.28^{155.88}_{155.732}$	$301330^{4949670}_{169820}$	$-125310^{62429}_{2329690}$	0.8883 ± 0.010678	0.37315 ± 0.0094545
$-91.15^{155.554}_{167.76}$	$179.78^{151.84}_{163.115}$	$572960^{1811940}_{267980}$	-33961^{5236}_{13049}	1.0576 ± 0.068604	0.3022 ± 0.00763

(This table is available in its entirety in machine-readable form.)

ORCID iDs

Sam Christian ● https://orcid.org/0000-0003-0046-2494
Andrew Vanderburg ● https://orcid.org/0000-0001-7246-5438
Juliette Becker ● https://orcid.org/0000-0002-7733-4522
Daniel A. Yahalomi ● https://orcid.org/0000-0003-4755-584X
Logan Pearce ● https://orcid.org/0000-0003-3904-7378
Karen A. Collins ● https://orcid.org/0000-0001-6588-9574
Adam L. Kraus ● https://orcid.org/0000-0001-9811-568X
Keivan G. Stassun ● https://orcid.org/0000-0002-3481-9052
Zoe de Beurs ● https://orcid.org/0000-0002-7564-6047
George R. Ricker ● https://orcid.org/0000-0003-2058-6662
Roland K. Vanderspek ● https://orcid.org/0000-0001-6763-6562
David W. Latham ● https://orcid.org/0000-0001-9911-7388
Joshua N. Winn ● https://orcid.org/0000-0002-4265-047X
S. Seager ● https://orcid.org/0000-0002-6892-6948
Jon M. Jenkins ● https://orcid.org/0000-0002-4715-9460
Pedro J. Amado ● https://orcid.org/0000-0001-8012-3788
David Baker ● https://orcid.org/0000-0002-2970-0532
Khalid Barkaoui ● https://orcid.org/0000-0003-1464-9276
Zouhair Benkhaldoun ● https://orcid.org/0000-0001-6285-9847
John Berberian ● https://orcid.org/0000-0003-1466-8389
Allyson Bieryla ● https://orcid.org/0000-0001-6637-5401
Emma Esparza-Borges ● https://orcid.org/0000-0002-2341-3233
Peyton Brown ● https://orcid.org/0000-0002-2546-9708
Lars A. Buchhave ● https://orcid.org/0000-0003-1605-5666
Christopher J. Burke ● https://orcid.org/0000-0002-7754-9486
Charles Cadieux ● https://orcid.org/0000-0001-9291-5555
Douglas A. Caldwell ● https://orcid.org/0000-0003-1963-9616
David Charbonneau ● https://orcid.org/0000-0002-9003-484X
Nikita Chazov ● https://orcid.org/0000-0002-4070-7831
Kevin I. Collins ● https://orcid.org/0000-0003-2781-3207
Dennis M. Conti ● https://orcid.org/0000-0003-2239-0567
Nicolas Crouzet ● https://orcid.org/0000-0001-7866-8738
Shila Deljookorani ● https://orcid.org/0000-0003-3548-0676
René Doyon ● https://orcid.org/0000-0001-5485-4675
Diana Dragomir ● https://orcid.org/0000-0003-2313-467X
Zahra Essack ● https://orcid.org/0000-0002-2482-0180
Phil Evans ● https://orcid.org/0000-0002-5674-2404
Akihiko Fukui ● https://orcid.org/0000-0002-4909-5763
Tianjun Gan ● https://orcid.org/0000-0002-4503-9705
Gilbert A. Esquerdo ● https://orcid.org/0000-0002-9789-5474
Michaël Gillon ● https://orcid.org/0000-0003-1462-7739
Pere Guerra ● https://orcid.org/0000-0002-4308-2339
Tristan Guillot ● https://orcid.org/0000-0002-7188-8428
Emmanuël Jehin ● https://orcid.org/0000-0001-8923-488X
Eric L. N. Jensen ● https://orcid.org/0000-0002-4625-7333
Marshall C. Johnson ● https://orcid.org/0000-0002-5099-8185
John H. Livingston ● https://orcid.org/0000-0002-4881-3620
John F. Kielkopf ● https://orcid.org/0000-0003-0497-2651
Vadim Krushinsky ● https://orcid.org/0000-0001-9388-691X
Pablo Lewin ● https://orcid.org/0000-0003-0828-6368
Bob Massey ● https://orcid.org/0000-0001-8879-7138

Mayuko Mori ● https://orcid.org/0000-0003-1368-6593
Kim K. McLeod ● https://orcid.org/0000-0001-9504-1486
Djamel Mékarnia ● https://orcid.org/0000-0001-5000-7292
Ismael Mireles ● https://orcid.org/0000-0002-4510-2268
Nikolay Mishevskiy ● https://orcid.org/0000-0001-8860-5861
Motohide Tamura ● https://orcid.org/0000-0002-6510-0681
Felipe Murgas ● https://orcid.org/0000-0001-9087-1245
Norio Narita ● https://orcid.org/0000-0001-8511-2981
Enric Palle ● https://orcid.org/0000-0003-0987-1593
Hannu Parviainen ● https://orcid.org/0000-0001-5519-1391
Peter Plavchan ● https://orcid.org/0000-0002-8864-1667
Francisco J. Pozuelos ● https://orcid.org/0000-0003-1572-7707
Markus Rabus ● https://orcid.org/0000-0003-2935-7196
Samuel N. Quinn ● https://orcid.org/0000-0002-8964-8377
Joshua E. Schlieder ● https://orcid.org/0000-0001-5347-7062
Richard P. Schwarz ● https://orcid.org/0000-0001-8227-1020
Avi Shporer ● https://orcid.org/0000-0002-1836-3120
Olga Suarez ● https://orcid.org/0000-0002-3503-3617
Chris Stockdale ● https://orcid.org/0000-0003-2163-1437
Thiam-Guan Tan ● https://orcid.org/0000-0001-5603-6895
Yuka Terada ● https://orcid.org/0000-0003-2887-6381
Amaury Triaud ● https://orcid.org/0000-0002-5510-8751
Rene Tronsgaard ● https://orcid.org/0000-0003-1001-0707
William C. Waalkes ● https://orcid.org/0000-0002-8961-0352
Gavin Wang ● https://orcid.org/0000-0003-3092-4418
Noriharu Watanabe ● https://orcid.org/0000-0002-7522-8195
Justin Wittrock ● https://orcid.org/0000-0002-7424-9891

References

Adams, F. C., Ruden, S. P., & Shu, F. H. 1989, ApJ, 347, 959
Andrews, S. M., Wilner, D. J., Hughes, A. M., Qi, C., & Dullemond, C. P. 2010, ApJ, 723, 1241
Angus, R., Morton, T. D., Foreman-Mackey, D., et al. 2019, AJ, 158, 173
Ansdell, M., Williams, J. P., Trapman, L., et al. 2018, ApJ, 859, 21
Antognini, J. M. O. 2015, MNRAS, 452, 3610
Barclay, T., Pepper, J., & Quintana, E. V. 2018, ApJS, 239, 2
Bate, M. R. 2018, MNRAS, 475, 5618
Bate, M. R., Bonnell, I. A., Clarke, C. J., et al. 2000, MNRAS, 317, 773
Batygin, K. 2012, Natur, 491, 418
Batygin, K., Bodenheimer, P. H., & Laughlin, G. P. 2016, ApJ, 829, 114
Bazsó, Á., & Pilat-Lohinger, E. 2020, AJ, 160, 2
Becker, J. C., & Adams, F. C. 2017, MNRAS, 468, 549
Becker, J. C., Vanderburg, A., Adams, F. C., Khain, T., & Bryan, M. 2017, AJ, 154, 230
Becker, J. C., Vanderburg, A., Adams, F. C., Rappaport, S. A., & Schwengeler, H. M. 2015, ApJL, 812, L18
Belokurov, V., Penoyre, Z., Oh, S., et al. 2020, MNRAS, 496, 1922
Blunt, S., Nielsen, E. L., De Rosa, R. J., et al. 2017, AJ, 153, 229
Blunt, S., Wang, J. J., Angelo, I., et al. 2020, AJ, 159, 89
Bonnell, I. A., & Bate, M. R. 1994, MNRAS, 271, 999
Bouma, L. G., Masuda, K., & Winn, J. N. 2018, AJ, 155, 244
Brown, T. M., Baliber, N., Bianco, F. B., et al. 2013, PASP, 125, 1031
Buchhave, L. A., & Latham, D. W. 2015, ApJ, 808, 187
Buchhave, L. A., Latham, D. W., Johansen, A., et al. 2012, Natur, 486, 375
Buchhave, L. A., Bizzarro, M., Latham, D. W., et al. 2014, Natur, 509, 593
Buder, S., Asplund, M., Duong, L., et al. 2018, MNRAS, 478, 4513
Cañas, C. I., Wang, S., Mahadevan, S., et al. 2019, ApJL, 870, L17
Casagrande, L., Schönrich, R., Asplund, M., et al. 2011, A&A, 530, A138
Chambers, K. C., Magnier, E. A., Metcalfe, N., et al. 2016, arXiv:1612.05560
Choi, J., Dotter, A., Conroy, C., et al. 2016, ApJ, 823, 102
Coelho, P., Barbuy, B., Meléndez, J., Schiavon, R. P., & Castilho, B. V. 2005, A&A, 443, 735
Collins, K. A., Kielkopf, J. F., Stassun, K. G., & Hessman, F. V. 2017, AJ, 153, 77
Correa-Otto, J. A., & Gil-Hutton, R. A. 2017, A&A, 608, A116

Čotar, K., Zwitter, T., Kos, J., et al. 2019, MNRAS, 483, 3196
D'Alessio, P., Calvet, N., Hartmann, L., Franco-Hernández, R., & Servín, H. 2006, ApJ, 638, 314
Dawson, R. I., & Johnson, J. A. 2018, ARA&A, 56, 175
Deacon, N. R., & Kraus, A. L. 2020, MNRAS, 496, 5176
Deacon, N. R., Kraus, A. L., Mann, A. W., et al. 2016, MNRAS, 455, 4212
Dimitrov, D. P., & Kjurkchieva, D. P. 2010, MNRAS, 406, 2559
Dotter, A. 2016, ApJS, 222, 8
Doyle, L. R., Carter, J. A., Fabrycky, D. C., et al. 2011, Sci, 333, 1602
Duchêne, G. 2010, ApJL, 709, L114
Eastman, J. 2017, EXOFASTv2: Generalized publication-quality exoplanet modeling code, Astrophysics Source Code Library, ascl:1710.003
Eastman, J. D., Brown, T. M., Hygelund, J., et al. 2014, Proc. SPIE, 9147, 436
El-Badry, K., & Rix, H.-W. 2018, MNRAS, 480, 4884
El-Badry, K., & Rix, H.-W. 2019, MNRAS, 482, L139
El-Badry, K., Rix, H.-W., & Heintz, T. M. 2021, MNRAS, 506, 2269
Fabrycky, D., & Tremaine, S. 2007, ApJ, 669, 1298
Fernández-López, M., Zapata, L. A., & Gabbasov, R. 2017, ApJ, 845, 10
Ferrer-Chávez, R., Wang, J. J., & Blunt, S. 2021,
Fűrész, G. 2008, PhD thesis, University of Szeged, Hungary, https://doktori.bibl.u-szeged.hu/id/eprint/1135
Fischer, D. A., & Marcy, G. W. 1992, ApJ, 396, 178
Frankowski, A., Jancart, S., & Jorissen, A. 2007, A&A, 464, 377
Fressin, F., Torres, G., Charbonneau, D., et al. 2013, ApJ, 766, 81
Gaia Collaboration, Prusti, T., de Bruijne, J. H. J., et al. 2016, A&A, 595, A1
Gaia Collaboration, Brown, A. G. A., Vallenari, A., et al. 2018, A&A, 616, A1
Gaia Collaboration, Brown, A. G. A., Vallenari, A., et al. 2021, A&A, 649, A1
Guerrero, N. M., Seager, S., Huang, C. X., et al. 2021, ApJS, 254, 39
Guillot, T., Abe, L., Agabi, A., et al. 2015, AN, 336, 638
Hawkins, K., Lucey, M., Ting, Y.-S., et al. 2020, MNRAS, 492, 1164
Hinkel, N. R., Timmes, F. X., Young, P. A., Pagano, M. D., & Turnbull, M. C. 2014, AJ, 148, 54
Hjorth, M., Albrecht, S., Hirano, T., et al. 2021, PNAS, 118, 2017418118
Holman, M., Touma, J., & Tremaine, S. 1997, Natur, 386, 254
Huang, C. X., Quinn, S. N., Vanderburg, A., et al. 2020, ApJL, 892, L7
Jensen, E. 2013, Tapir: A web Interface for Transit/eclipse Observability, Astrophysics Source Code Library, ascl:1306.007
Jiménez-Esteban, F. M., Solano, E., & Rodrigo, C. 2019, AJ, 157, 78
Kaib, N. A., Raymond, S. N., & Duncan, M. 2013, Natur, 493, 381
Koch, D. G., Borucki, W. J., Basri, G., et al. 2010, ApJL, 713, L79
Kouwenhoven, M. B. N., Goodwin, S. P., Parker, R. J., et al. 2010, MNRAS, 404, 1835
Kozai, Y. 1962, AJ, 67, 591
Kraus, A. L., Ireland, M. J., Huber, D., Mann, A. W., & Dupuy, T. J. 2016, AJ, 152, 8
Kunder, A., Kordopatis, G., Steinmetz, M., et al. 2017, AJ, 153, 75
Lai, D. 2014, MNRAS, 440, 3532
Latham, D. W., Mazeh, T., Davis, R. J., Stefanik, R. P., & Abt, H. A. 1991, AJ, 101, 625
Lee, K. I., Dunham, M. M., Myers, P. C., et al. 2016, ApJL, 820, L2
Li, D., Mustill, A. J., & Davies, M. B. 2020, MNRAS, 499, 1212
Lidov, M. L. 1962, P&SS, 9, 719
Lin, D. N. C., Bodenheimer, P., & Richardson, D. C. 1996, Natur, 380, 606
Lindegren, L. 2018, DPAC, GAIA-C3-TN-LU-LL-124-01, http://www.rssd.esa.int/doc_fetch.php?id=3757412
Lindegren, L., Hernández, J., Bombrun, A., et al. 2018, A&A, 616, A2
Lindegren, L., Klioner, S. A., Hernández, J., et al. 2021, A&A, 649, A2
Majewski, S. R. & APOGEE Team 2016, AN, 337, 863
Mamajek, E. E. 2009, in AIP Conf. Ser. 1158, Exoplanets and Disks: Their Formation and Diversity, ed. T. Usuda, M. Tamura, & M. Ishii (Melville, NY: AIP), 3
Manara, C. F., Tazzari, M., Long, F., et al. 2019, A&A, 628, A95
Mann, A. W., Dupuy, T., Kraus, A. L., et al. 2019, ApJ, 871, 63
Martin, R. G., & Lubow, S. H. 2017, ApJL, 835, L28
Mason, B. D., Wycoff, G. L., Hartkopf, W. I., Douglass, G. G., & Worley, C. E. 2001, AJ, 122, 3466

Mink, D. J. 2011, in ASP Conf. Ser. 442, Astronomical Data Analysis Software and Systems XX, ed. I. N. Evans et al. (San Francisco, CA: ASP), 305
Morton, T. D. 2015, isochrones: Stellar model grid package, Astrophysics Source Code Library, ascl:1503.010
Morton, T. D., & Johnson, J. A. 2011, ApJ, 738, 170
Mugrauer, M. 2019, MNRAS, 490, 5088
Mugrauer, M., & Michel, K. U. 2020, AN, 341, 996
Murray, C. D., & Dermott, S. F. 1999, Solar System Dynamics (Cambridge: Cambridge Univ. Press)
Nagayama, T., Nagashima, C., Nakajima, Y., et al. 2003, Proc. SPIE, 4841, 459
Naoz, S., Farr, W. M., Lithwick, Y., Rasio, F. A., & Teyssandier, J. 2013, MNRAS, 431, 2155
Naoz, S., Farr, W. M., & Rasio, F. A. 2012, ApJL, 754, L36
Narita, N., Fukui, A., Kusakabe, N., et al. 2015, JATIS, 1, 045001
Narita, N., Fukui, A., Kusakabe, N., et al. 2019, JATIS, 5, 015001
Narita, N., Fukui, A., Yamamuro, T., et al. 2020, Proc. SPIE, 11447, 114475K
Nelson, A. F., Benz, W., & Ruzmaikina, T. V. 2000, ApJ, 529, 357
Newton, E. R., Mann, A. W., Tofflemire, B. M., et al. 2019, ApJL, 880, L17
Ngo, H., Knutson, H. A., Hinkley, S., et al. 2016, ApJ, 827, 8
Offner, S. S. R., Dunham, M. M., Lee, K. I., Arce, H. G., & Fielding, D. B. 2016, ApJL, 827, L11
Offner, S. S. R., Kratter, K. M., Matzner, C. D., Krumholz, M. R., & Klein, R. I. 2010, ApJ, 725, 1485
Pearce, L. A., Kraus, A. L., Dupuy, T. J., et al. 2020, ApJ, 894, 115
Petigura, E. 2015, arXiv:1510.03902
Petigura, E. A., Howard, A. W., Marcy, G. W., et al. 2017, AJ, 154, 107
Petrovich, C. 2015, ApJ, 799, 27
Price-Whelan, A. M., Sipőcz, B. M., Günther, H. M., et al. 2018, AJ, 156, 123
Raghavan, D., McAlister, H. A., Henry, T. J., et al. 2010, ApJS, 190, 1
Ricker, G. R., Winn, J. N., Vanderspek, R., et al. 2015, JATIS, 1, 014003
Riddell, A., Hartikainen, A., Lee, D., et al. 2018, stan-dev/pystan: v2.18.0.0, v2.18.0.0, Zenodo, doi:10.5281/zenodo.1456206
Santerne, A., Díaz, R. F., Moutou, C., et al. 2012, A&A, 545, A76
Schwab, C., Spronck, J. F. P., Tokovinin, A., & Fischer, D. A. 2010, Proc. SPIE, 7735, 77354G
Sigalotti, L. D. G., Cruz, F., Gabbasov, R., Klapp, J., & Ramírez-Velasquez, J. 2018, ApJ, 857, 40
Siverd, R., Brown, T. M., Henderson, T., et al. 2017, AAS Meeting Abstracts, 230, 102.07
Siverd, R. J., Brown, T. M., Barnes, S., et al. 2018, Proc. SPIE, 10702, 1918
Skrutskie, M. F., Cutri, R. M., Stiening, R., et al. 2006, AJ, 131, 1163
Spada, F., Demarque, P., Kim, Y. C., & Sills, A. 2013, ApJ, 776, 87
Stassun, K. G., Corsaro, E., Pepper, J. A., & Gaudi, B. S. 2018, AJ, 155, 22
Stassun, K. G., Oelkers, R. J., Paegert, M., et al. 2019, AJ, 158, 138
Steinmetz, M. 2003, in ASP Conf. Ser. 298, GAIA Spectroscopy: Science and Technology, ed. U. Munari (San Francisco, CA: ASP), 381
Sterne, T. E. 1939, MNRAS, 99, 451
Taylor, M. B. 2006, in ASP Conf. Ser. 351, Astronomical Data Analysis Software and Systems XV, ed. C. Gabriel (San Francisco, CA: ASP), 666
Telting, J. H., Avila, G., Buchhave, L., et al. 2014, AN, 335, 41
Tobin, J. J., Chandler, C. J., Wilner, D. J., et al. 2013, ApJ, 779, 93
Tobin, J. J., Looney, L. W., Li, Z.-Y., et al. 2016, ApJ, 818, 73
Tokovinin, A. 2017, MNRAS, 468, 3461
Tokovinin, A., Fischer, D. A., Bonati, M., et al. 2013, PASP, 125, 1336
von Zeipel, H. 1910, AN, 183, 345
Wallraff, H. G. 1979, Behavioral Ecology and Sociobiology, 5, 201
Watson, G. 1983, Canadian Mathematical Society Series of Monographs and Advanced Texts (New York: Wiley)
Weiss, L. M., Deck, K. M., Sinukoff, E., et al. 2017, AJ, 153, 265
Wu, Y., & Murray, N. 2003, ApJ, 589, 605
Zanazzi, J. J., & Lai, D. 2018, MNRAS, 477, 5207
Zhao, G., Zhao, Y.-H., Chu, Y.-Q., Jing, Y.-P., & Deng, L.-C. 2012, RAA, 12, 723
Ziegler, C., Tokovinin, A., Briceño, C., et al. 2020, AJ, 159, 19
Ziegler, C., Tokovinin, A., Latiolais, M., et al. 2021, AJ, 162, 192